Journal of Statistical Physics, Vol. 93, Nos. 3/4, 1998

Axisymmetric Surface Diffusion: Dynamics and Stability of Self-Similar Pinchoff

Andrew J. Bernoff,[1,2] Andrea L. Bertozzi,[1] and Thomas P. Witelski[1]

Received February 3, 1998; final August 3, 1998

The dynamics of surface diffusion describes the motion of a surface with its normal velocity given by the surface Laplacian of its mean curvature. This flow conserves the volume enclosed inside the surface while minimizing its surface area. We review the axisymmetric equilibria: the cylinder, sphere, and the Delaunay unduloid. The sphere is stable, while the cylinder is long-wave unstable. A subcritical bifurcation from the cylinder produces a continuous family of unduloid solutions. We present computations that suggest that the stable manifold of the unduloid forms a separatrix between states that relax to the cylinder in infinite time and those that tend toward finite-time pinchoff. We examine the structure of the pinchoff, showing it has self-similar structure, using asymptotic, numerical, and analytical methods. In addition to a previously known similarity solution, we find a countable set of similarity solutions, each with a different asymptotic cone angle. We develop a stability theory in similarity variables that selects the original similarity solution as the only linearly stable one and consequently the only observable solution. We also consider similarity solutions describing the dynamics after the topological transition.

KEY WORDS: surface diffusion; similarity solution; Pinchoff; linear stability.

1. INTRODUCTION

In a closed isotropic system surface diffusion preserves the volume of the solid while reducing its surface area, analogous to the classical Rayleigh instability of a cylinder of a fluid under capillary forces. For both problems, cylindrical surfaces pinchoff to form chains of spheres that minimize the

[1] Department of Mathematics, Duke University, Durham, North Carolina 27708; e-mail: bertozzi@math.duke.edu, witelski@math.duke.edu.

[2] Current address: Department of Mathematics, Harvey Mudd College, Claremont, California 91711; e-mail: ajb@hmc.edu.

0022-4715/98/1100-0725$15.00/0

surface area per volume. This phenomenon is observed in many physical systems with application to such fields as integrated circuit technology, annealing, and sintering. When a solid is heated, atoms at the outer surface can become mobile at a temperature well below the melting temperature. Such atoms diffuse to form a thermodynamically lower energy configuration and, in the process, cause a mass flux from regions of high surface energy to lower surface energy. When the characteristic mean-free path of a surface atom is small compared to the characteristic dimension of the sample, the average normal velocity U of the surface is proportional to the surface Laplacian of the sum of the principal curvatures (the normalized mean curvature),

$$U = \nabla_s^2 \mathscr{H} \tag{1.1}$$

In this paper we investigate the dynamics of these surfaces, concentrating on the dynamics of pinchoff, using a combination of numerical, analytical and asymptotic techniques.

Based on the earlier work of Herring [Her51], Mullins derived equation (1.1) in [Mul57] and recently reviewed the detailed physics of mass transport on surfaces in [Mul95]. Mullins' derivation, which we review in Section 2, assumes that the mean-free path of the diffusing particles is small compared to the sample size. Cahn and Taylor [CT94] generalize this model to include both anisotropy and cases where surface diffusion is much faster than the attachment kinetics (i.e., the limit of large mean-free path). The reader is also referred to [CFM96, CFM95] for some discussion of the model.

Motion via surface diffusion preserves volume and dissipates surface area [CT94]. In studying capillary instability in fluid dynamics, Rayleigh first addressed the problem of minimizing surface area for a fixed volume. Surfaces of constant mean curvature are both extrema for the capillary minimization problem and steady states for the surface diffusion problem. In Section 2, we show that those surfaces that minimize surface area are precisely the same as the linearly stable equilibria under surface diffusion. This allows us to use previously known results [Fin86, Vog87, Vog89, FV92, Zho93] for the capillary minimization problem to classify steady states for the surface diffusion problem.

As we show in Section 3 for the axisymmetric case, Eq. (1.1) yields a fourth-order nonlinear diffusion equation for motion of the surface. Mullins original investigation [Mul57] of surface diffusion concentrated on understanding the appearance of a groove at a grain boundary of a heated polycrystalline material. He derived a self-similar solution of a linearized near-planar version of (1.1) where lengths scale as $(time)^{1/4}$, reflecting the

fourth-order diffusive nature of the problem. In a subsequent investigation [Mul59] he estimated the rate at which perturbations to a planar surface flatten, again finding a $(time)^{1/4}$ self-similar rescaling of perturbation amplitudes and widths.

For the general surface diffusion problem, very few analytical results are known. Due to the lack of a maximum principle, at best, we expect smooth solutions to exist only locally in time. Some results are known for the analogous flow of a curve in a plane [BDR84, AL98, EG97, CT94]. More recent results for the surfaces in $\mathbb{R}^n$ [EMS97, EMS98] prove local existence, regularity, and local convergence to the sphere.

The long time evolution of a surface evolving via (1.1) can be limited by topological changes of surface, including self-intersections of the surface (local "coalescence") in either two or three dimensions or the pinchoff of a connected tube-like structure in three dimensions. Coalescence of initially separated parts of the surface may occur due to the locality of the surface dynamics and lack of a maximum principle [CT94]. When such coalescences occur in three dimensions, as in the case of two spherical surfaces touching, the ensuing dynamics can be quite complex [Egg98]. In the case of pinchoff, previous numerical work [NM65a, NM65b, SM82, MS79, CFM96, CFM95] suggests that axisymmetric tubes can form such singularities leading to changes in topology. Although one can suggest ways to continue the solution after the topology change [CFM96, CFM95, WMVD98], uniqueness of this continuation is not known. Cahn and Taylor [CT94] discuss various strategies for mollifying these difficulties.

Nichols and Mullins [NM65a, NM65b] investigated numerically the evolution of axisymmetric solutions of the surface diffusion equation in connection with various applications. They derive the Rayleigh criteria for stability of a cylinder; namely that it is unstable to perturbations with wavelengths greater than 2π times itstradius. They suggest that this Rayleigh instability leads to a pinchoff of the cylinder. These ideas were studied further by Marinas and Sekerka [MS79, SM82]. In Section 3 we take these ideas one step further. After reviewing the stability theory of Nichols and Mullins for the cylinder and sphere, where the eigenvalues can be computed analytically, we consider a third class of axisymmetric equilibria, the unduloid. We show that the unduloids form a branch of solutions that bifurcate subcritically from the cylinder at the critical cylinder length of $2\pi r$. Each unduloid has a stable manifold of codimension one that divides phase space into states that evolve towards the cylinder or evolve towards a finite-time pinchoff.

Coleman, Falk and Moakher [CFM96, CFM95] demonstrated numerically that a cylinder subject to an axially symmetric perturbation can show pinchoff in finite time. The conical nature of this pinchoff is evident in their

computations. In addition, they use surface "surgery" to numerically change the topology of the surface near pinchoff in order to compute a solution after pinchoff. They follow the evolution from a perturbed cylinder, through pinchoff, to a series of disconnected spheres that is clearly a local minimizer of surface area. Their numerical work suggests a universal cone angle upon pinchoff, however they compute on fixed uniform grids so it is difficult to measure precisely the cone angle near pinchoff or the precise dynamics of the pinchoff, which occurs on decreasingly smaller scales.

Since the work of Coleman, Falk and Moakher [CFM96, CFM95], Wong, Miksis, Voorhees, and Davis studied surface diffusion in a series of four papers [WMD97, WVMD97, MVM+96, WMVD98]. In the fourth paper [WMVD98] they examine the self-similar axisymmetric pinchoff of a cylinder. The surface diffusion equation is rescaled into self-similar coordinates, where lengths are scaled as the fourth root of the time to pinchoff. They numerically compute a solution of the resulting ODE, using a shooting method. Their solution has a half-cone angle of 46.04°, which compares very favorably with the previous studies [NM65a, CFM96, SM82]. This result can be thought of as the starting point for the present study.

Self-similarity in topological transitions for interfaces has become the topic of much research during the past decade [Kad97]. Eggers [Egg93] shows that droplet pinchoff has a universal self-similar form. Subsequent work of Brenner *et al.* [BLS96] found a countably infinite set of such similarity solutions, with the "ground state" given by Eggers. This prompted us to look for the same structure in the problem of self-similar pinchoff via surface diffusion. We show, in Section 4, that there are indeed a countably infinite number of similarity solutions describing pinchoff. Our "ground state" is the similarity solution found in [WMVD98]. We compare the results for the similarity solutions with fully nonlinear computations of the surface evolution equation. In order to resolve the scaling structure of the pinchoff over many lengthscales, we use a self-similar adaptive mesh-refinement procedure similar to that used in [Ber96]. We find that regardless of the initial condition, the computations always show pinchoff that has the local structure of the "ground state."

In Section 5, we explain why the ground state is the only observable one in the computations of Section 4. Via a linear stability analysis in similarity variables, we show that, modulo eigenvalues associated with time and space translation in the original system, that the ground state is the only linearly stable similarity solution. We also show that this state is linearly stable to nonaxisymmetric perturbations, making it a likely candidate to describe nonaxisymmetric pinchoff of tubes. In Section 6, we consider the existence and stability of solutions after pinchoff. We find a continuous family of stable similarity solutions parametrized by the far-field

cone angle. These results suggest that the continuation after pinchoff is unique and stable.

2. FORMULATION OF MODEL

In this section we derive some basic identities for motion by surface diffusion. Consider a solid occupying a volume Ω with boundary $\partial\Omega$. Associated with each point on the surface are two *principal curvatures*, κ_1 and κ_2 whose sum is $\mathscr{H}$, the normalized mean curvature,[3] and whose product is $\mathscr{Q}$, the Gaussian curvature. If the chemical potential is proportional to the surface area, then the change in chemical potential due to the displacement of a single surface atom is proportional to the mean curvature, $\mathscr{H}$. Thermodynamically, the surface atoms move towards the potential minimum. Consequently, the volume flux of surface atoms $\vec{Q}$ is proportional to the surface gradient of the curvature,

$$\vec{Q} \equiv -\nabla_s \mathscr{H} \tag{2.1}$$

where without loss of generality we assume the mobility (constant of proportionality) to be one. Conservation of mass in a test volume on the surface [Ari62] dictates that the normal velocity, U, of the surface equals the divergence of the flux,

$$U = -\nabla_s \cdot \vec{Q} = \nabla_s^2 \mathscr{H} \tag{2.2}$$

The surface of the solid $\vec{\Gamma}(p_1, p_2, t)$ is parametrized (at least locally) by two Lagrangian surface coordinates p_1, p_2 and evolves in time, t,

$$\frac{d\vec{\Gamma}}{dt} = U\hat{n} \tag{2.3}$$

with a normal velocity (2.2) equal to the surface Laplacian of the mean curvature, $\mathscr{H}$, where $\hat{n}$ is an inward pointing surface normal. For the purpose of this section, we consider $\vec{\Gamma}$ to be a compact, connected, oriented Riemannian manifold without boundaries. This includes the case of an axisymmetric surface, periodic along the axis of symmetry, which is the subject of the remaining sections of the paper. However many of the results stated here also easily generalize to surfaces with boundaries, such as those that model the surface diffusion of a solid film on an impermeable substrate (see, for example, [WMD97, MVM+96, Mu195]). This is particularly relevant

[3] We refer to the normalized mean curvature throughout the paper as simply the mean curvature, although it is actually twice the average (mean) of the principal curvatures. We use the convention that curvature is positive on spheres, consistent with [CFM96, CFM95].

for understanding the stability of conducting traces on an insulating substrate for integrated circuits [MVM+96]. For the geometric identities used below, the reader is directed to the book of Aris [Ari62]. Later in this paper, we restrict ourselves to surfaces that are axisymmetric and periodic in the direction of the axis of symmetry.

2.1. Volume Conservation and Area Dissipation

We begin by reviewing the fact that evolution via surface diffusion conserves volume and dissipates surface area [CT94]. The rate of change of the volume, $\mathcal{V}(t)$, of Ω is the integral of the normal velocity over the surface ([Ari62], p. 178),

$$\frac{d\mathcal{V}}{dt} = \int_{\partial\Omega} U \, dS \tag{2.4}$$

Substituting (2.2), and applying the surface divergence theorem yields conservation of volume,

$$\frac{d\mathcal{V}}{dt} = 0 \qquad \mathcal{V}(t) \equiv \mathcal{V}_0 \tag{2.5}$$

where the initial volume, $\mathcal{V}_0$, is specified by the initial condition. The rate of change of the surface area $\mathcal{A}(t)$ is

$$\frac{d\mathcal{A}}{dt} = \frac{d}{dt} \int_{\partial\Omega} dS$$

To compute this time derivative on the right hand side, we note, from (2.3), that moving the interface from $\vec{\Gamma}$ to $\vec{\Gamma} + U\hat{n}\,dt$ changes an infinitesimal surface element dS by ([Ari62], Chap. 10)

$$dS \to (1 + U\mathcal{H}\,dt)\, dS \tag{2.6}$$

Hence

$$\frac{d\mathcal{A}}{dt} = \int_{\partial\Omega} U\mathcal{H} \, dS \tag{2.7}$$

Substituting the normal velocity (2.2), and applying the divergence theorem yields,

$$\frac{d\mathcal{A}}{dt} = -\int_{\partial\Omega} |\nabla_s \mathcal{H}|^2 \, dS \leqslant 0 \tag{2.8}$$

which shows that, for all surface diffusion motion, surface area is non-increasing. Moreover, *the surface area is strictly decreasing for all surfaces except equilibrium surfaces of constant mean curvature.*

2.2. The H^{-1} Inner-Product

We gain some insight into the dynamics and stability of perturbed equilibria by formulating the surface diffusion problem as a gradient flow in an H^{-1} inner-product. This method arises in Cahn–Hilliard type problems and was first extended to the motion of surfaces by Cahn and Taylor [CT94]. Our presentation follows the discussion in Taylor and Cahn [TC94].

First we note that any zero mean function $w(p_1, p_2)$ on the surface,

$$\int_{\partial\Omega} w\, dS = 0 \tag{2.9}$$

has a unique zero mean potential, Φ_w, such that [War83]

$$\nabla_s^2 \Phi_w = w \tag{2.10}$$

Now define the H^{-1} inner-product, on the surface $\partial\Omega$, of two zero-mean functions w, v, as

$$\begin{aligned} \langle w, v\rangle_{H^{-1}} &\equiv \int_{\partial\Omega} \nabla_s \Phi_w \cdot \nabla_s \Phi_v\, dS \\ &= -\int_{\partial\Omega} w\Phi_v\, dS \\ &= -\int_{\partial\Omega} v\Phi_w\, dS \end{aligned}$$

a positive definite bilinear form on the zero-mean functions w and v.

Using this inner product, surface area dissipation (2.7) can be written as

$$\frac{d\mathcal{A}}{dt} = -\langle U, \nabla_s^2 \mathcal{H}\rangle_{H^{-1}} \tag{2.11}$$

From Schwarz's inequality, it follows that the surface diffusion evolution, $U = \nabla_s^2 \mathcal{H}$, maximizes the rate of surface area dissipation among all velocity laws of the same L^2 norm. This leads to Taylor and Cahn's [CT94] recognition of this flow as a gradient flow in the H^{-1} norm.

2.3. Equilibrium Shapes and Their Linear Stability

From the dissipation of surface area (2.7), equilibrium shapes have constant mean curvature, $\mathscr{H} = \mathscr{H}_0$. In this paper, we discuss the axisymmetric equilibrium surfaces (cylinders, spheres and Delaunay unduloids). In order to understand the dynamics of axisymmetric surfaces, we must examine their stability under perturbation.

Suppose $\vec{\Gamma}_0(p_1, p_2)$ is an equilibrium surface with constant mean curvature, $\mathscr{H}(\vec{\Gamma}_0) = \mathscr{H}_0$. Any small surface deformation can be measured by the displacement in the normal direction,

$$\vec{\Gamma}(p_1, p_2, t) = \vec{\Gamma}_0(p_1, p_2) + \gamma(p_1, p_2, t)\,\hat{n} \tag{2.12}$$

To linear order in γ, volume conservation imposes the restriction

$$\int_{\partial\Omega} \gamma \, dS = 0 \tag{2.13}$$

To linearize the surface diffusion evolution (2.3)

$$\frac{d\vec{\Gamma}}{dt} = \nabla_s^2 \mathscr{H} \tag{2.14}$$

about the steady state $\vec{\Gamma}_0$, a surface of constant mean curvature, we first compute the linear variation in the mean curvature due to the perturbation $\gamma\hat{n}$ (cf. [SB95, Dre90])

$$\mathscr{H}(\vec{\Gamma}_0 + \gamma\hat{n}) = \mathscr{H}_0 - (\nabla_s^2 + \kappa_1^2 + \kappa_2^2)\,\gamma + \mathcal{O}(\gamma^2) \tag{2.15}$$

where κ_1 and κ_2 are the principal curvatures of $\mathscr{H}_0$. The surface Laplacian ∇_s^2 depends on the perturbation γ, however since $\nabla_s^2 \mathscr{H}_0 = 0$ identically for any constant $\mathscr{H}_0$, the leading order contribution of $\nabla_s^2 \mathscr{H}$ due to the perturbation of the Laplacian enters at $\mathcal{O}(\gamma^2)$. Consequently the linearization of the surface diffusion equation (2.14) about $\vec{\Gamma}_0$ is:

$$\frac{\partial \gamma}{\partial t} = \mathscr{L}\gamma = -\nabla_s^2(\nabla_s^2 + \kappa_1^2 + \kappa_2^2)\,\gamma \tag{2.16}$$

In Section 3 we use (2.16) to compute the spectrum of the linearization about axisymmetric surfaces.

One advantage of working in the surface coordinates is now evident —the linearized operator is self-adjoint in the H^{-1} inner-product. This can

be shown by a straightforward computation. Consequently, *the eigenvalues of $\mathscr{L}$ are real*, generalizing an observation of Wong *et al.* [WMVD98, WVMD97] for certain special geometries.

The eigenvalue problem

$$\mathscr{L}\hat{\gamma}_n = \lambda_n \hat{\gamma}_n \tag{2.17}$$

can now be analyzed via a Rayleigh quotient [But68]. Because the operator is self-adjoint and the surface is compact, the spectrum is real and discrete. If the eigenvalues are ordered $\lambda_0 \geqslant \lambda_1 \cdots \geqslant \lambda_n \cdots$, then a Rayleigh quotient gives the largest eigenvalue

$$\lambda_0 = \max_{\gamma} \frac{\int_{\partial\Omega} (\kappa_1^2 + \kappa_2^2)\, \gamma^2 - |\nabla_s \gamma|^2 \, dS}{\langle \gamma, \gamma \rangle_{H^{-1}}} \tag{2.18}$$

where, again, γ is a zero-mean perturbation.

The linear operator has several zero eigenvalues, associated with physical symmetries of the problem, in particular infinitesimal translations and rotations. If λ_0 is strictly greater than zero, the equilibrium surface of constant mean curvature, $\vec{\Gamma}_0$, is linearly unstable.

In the next subsection we use the formula for the Rayleigh quotient to show that stable surfaces are the ones that are local minimizers of surface area.

2.4. Stability of Equilibria and Capillary Minimization

In the previous subsection, we reviewed the fact that evolution via surface diffusion minimizes surface area while conserving volume. The only equilibrium surfaces are those of constant mean curvature. Thus the only stable equilibria are constant mean curvature surfaces that locally minimize surface area. We now address the analytical connection between the linear stability of equilibria under surface diffusion and the following:

Capillary Minimization Problem: Given a fixed interior volume $\mathscr{V}_0$, find the surfaces that extremize surface area $\mathscr{A}$ and determine which are local minimizers of surface area.

Like the equilibrium surfaces for evolution via surface diffusion, the extremal surfaces in the capillary minimization problem have constant mean curvature (cf. [Fin86]), a fact that we rederive below. We also show that for the capillary minimization problem, the second variation of surface area is an expression that is equivalent to the Rayleigh quotient in (2.18), used to compute stability of equilibria for surface diffusion. Thus there is

a clear one-to-one correspondence between the stability of equilibria under surface diffusion, and the nature of the extrema for the capillary minimization problem. This allows us to use well known results for the capillary minimization problem to completely classify all equilibrium surfaces for the surface diffusion problem.

Following Vogel [Vog87], we solve the capillary minimization problem via the calculus of variations. Consider an *extremal* surface $\vec{\Gamma}_0$ for the capillary minimization problem, perturbed so that the interior volume is conserved:

$$\vec{\Gamma}(p_1, p_2) = \vec{\Gamma}_0(p_1, p_2) + \varepsilon\gamma_1(p_1, p_2)\,\hat{n} + \varepsilon^2\gamma_2(p_1, p_2)\,\hat{n} + \mathcal{O}(\varepsilon^3) \tag{2.19}$$

where γ_1 and γ_2 represent arbitrary perturbations to the surface.

Applying the volume constraint, we find

$$\mathcal{V} = \mathcal{V}(\vec{\Gamma}_0) + \varepsilon \int_{\partial\Omega} \gamma_1\, dS + \varepsilon^2 \int_{\partial\Omega} \gamma_2 + \tfrac{1}{2}\mathcal{H}(\vec{\Gamma}_0)\,\gamma_1^2\, dS + \mathcal{O}(\varepsilon^3) \tag{2.20}$$

where we employ (2.6) to expand the surface element. At leading order we verify that $\mathcal{V}(\vec{\Gamma}_0) = \mathcal{V}_0$. At $\mathcal{O}(\varepsilon)$, γ_1 is restricted to have zero mean,

$$\int_{\partial\Omega} \gamma_1\, dS = 0 \tag{2.21}$$

corresponding to a vanishing perturbation to the volume (2.13). At $\mathcal{O}(\varepsilon^2)$, γ_2 compensates for the second-order contribution to the volume from γ_1,

$$\gamma_2 = -\tfrac{1}{2}\mathcal{H}(\vec{\Gamma}_0)\,\gamma_1^2 + \sigma_2 \tag{2.22}$$

where σ_2 is an arbitrary zero-mean function.

Substituting (2.19) into the surface area functional and expanding yields

$$\mathcal{A}(\vec{\Gamma}) = \mathcal{A}_0 + \varepsilon\mathcal{A}_1 + \varepsilon^2\mathcal{A}_2 + \mathcal{O}(\varepsilon^3) \tag{2.23}$$

where

$$\mathcal{A}_0 = \mathcal{A}(\vec{\Gamma}_0)$$

$$\mathcal{A}_1 = \int_{\partial\Omega} \mathcal{H}(\vec{\Gamma}_0)\,\gamma_1\, dS$$

$$\mathcal{A}_2 = \int_{\partial\Omega} \tfrac{1}{2}\mathcal{H}^2(\vec{\Gamma}_0)\,\gamma_1^2 + \mathcal{H}(\vec{\Gamma}_0)\,\gamma_2 - \tfrac{1}{2}\gamma_1(\nabla_s^2 + \kappa_1^2 + \kappa_2^2)\,\gamma_1\, dS$$

and we use (2.6) and (2.15) to expand the surface area element and the mean-curvature respectively.

At $\mathcal{O}(\varepsilon)$, we derive the conditions for $\vec{\Gamma}_0$ to be extremal, namely that $\mathscr{A}_0$ vanishes,

$$\int_{\partial\Omega} \mathscr{H}(\vec{\Gamma}_0)\, \gamma_1\, dS = 0$$

where γ_1 is an arbitrary perturbation that satisfies the zero-mean condition (2.21). From this we deduce the well-known result that *extremal surfaces for the capillary minimization problem have constant mean curvature*, $\mathscr{H} = \mathscr{H}_0$, just as we deduced for the steady solutions of the surface diffusion problem.

At $\mathcal{O}(\varepsilon^2)$, substituting for γ_2 from the volume constraint (2.22) and applying the divergence theorem yields

$$\mathscr{A}_2 = \tfrac{1}{2} \int_{\partial\Omega} |\nabla_s \gamma_1|^2 - (\kappa_1^2 + \kappa_2^2)\, \gamma_1^2\, dS \tag{2.25}$$

where γ_1 is a zero-mean function. The surface $\vec{\Gamma}_0$ is a local minimizer of surface area if $\mathscr{A}_2 \geqslant 0$ for all γ_1. Moreover, the set of perturbations where $\mathscr{A}_2$ vanishes correspond exactly to infinitesimal translation and rotation symmetries.

Comparing (2.25) with equation (2.18), we recognize $\mathscr{A}_2$ as minus half the numerator of the Rayleigh quotient. Consequently, if $\mathscr{A}_2$ is negative, the extremal surface is unstable under the action of surface diffusion. Moreover, the space of perturbations for which $\mathscr{A}_2$ vanishes is exactly the null-space of $\mathscr{L}$, the linearized surface diffusion operator, both of which may be associated with the physical symmetries of the problem. Consequently, we conclude that *a constant mean curvature surface is linearly stable under evolution via surface diffusion if and only if it is a local minimizer for the volume-constrained capillary problem.*

This fact means that we can use the results of Vogel, Finn and Zhou [Vog87, Vog89, FV92, Zho93], for the capillary minimization problem, to classify the equilibrium surfaces for surface diffusion and their stability. In particular, this tells us that spheres are always linearly stable under surface diffusion and cylinders are always short-wave stable and long-wave unstable (with the critical wavelength equal to $2\pi r$, where r is the radius of the cylinder). A third axisymmetric surface, the Delaunay unduloid [BSS94, Del41], is a saddle point for the capillary minimization problem. Thus, we know that the unduloids are all linearly unstable under evolution via surface diffusion.

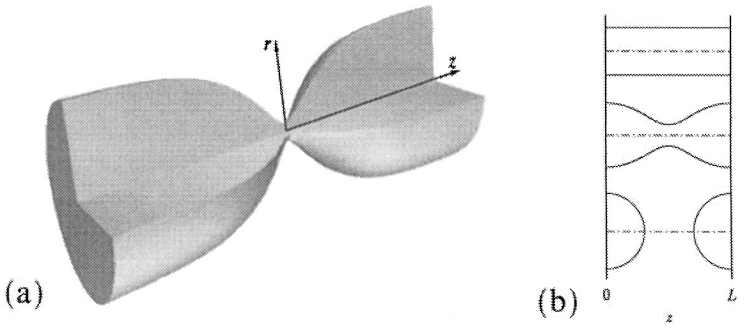

Fig. 1. (a) The geometry for cylinder approaching axisymmetric pinch-off. (b) Cross-sections of axisymmetric surfaces of constant mean curvature of equal volume on a finite interval of length L; a cylinder, one period of a Delaunay unduloid of revolution, and two hemispheres (from top to bottom, respectively).

Section 3 addresses in detail the linear and nonlinear stability of equilibria for the axisymmetric surface diffusion problem. In Section 3.1, we review the linear stability calculation of the well known axisymmetric examples, the cylinder and the sphere. For these examples, the full spectrum of the linear operator in (2.16) can be computed analytically. Also in that section, using numerical computation via inverse iteration, we compute the most unstable mode of the the linearization about the Delaunay unduloids. In Section 3.2 we show that for surface diffusion, the Delaunay unduloids form an unstable branch of solutions that bifurcates subcritically from the cylinder and reconnects to the sphere in a singular limit, involving a change of topology.

3. DIFFUSION OF AXISYMMETRIC SURFACES

In this section, we introduce the equation of motion for an axisymmetric surface that is a radial graph of a function $r = r(z)$ of the axial coordinate z (see Fig. 1a). There are three families of equilibria for which the function r is periodic in z: (see Fig. 1b), the *cylinder*, the *Delaunay unduloid*, and the *sphere*.[4] This section concerns the dynamics of solutions near these equilibrium states. First, we review the linear stability of these surfaces of revolution. Then, via bifurcation theory and numerical computations, we explore the dynamics near the unduloid surface, showing that it divides

[4] Note that the islolated sphere is a special case; it is not topologically equivalent to the cylinder or the unduloid on the interval, however it arises naturally as an extremum in the capillary minimization problem and as the limiting surface of the family of unduloids.

phase space into states that eventually relax to the cylinder and states that undergo a topological transition through a pinch-off singularity.

Consider the graph of a function $r = r(\theta, z, t)$ of the axial coordinate z and the angular coordinate θ. In these coordinates, the equation of motion (2.3) reduces to

$$\frac{r}{q}\frac{\partial r}{\partial t} = \nabla_s^2 \mathscr{H}, \qquad q = \sqrt{r^2(1+r_z^2)+r_\theta^2} \tag{3.1}$$

where the surface Laplacian is

$$\nabla_s^2 = \frac{1}{q}\left[\frac{\partial}{\partial z}\left(\frac{r^2+r_\theta^2}{q}\frac{\partial}{\partial z} - \frac{r_z r_\theta}{q}\frac{\partial}{\partial \theta}\right) + \frac{\partial}{\partial \theta}\left(\frac{1+r_z^2}{q}\frac{\partial}{\partial \theta} - \frac{r_z r_\theta}{q}\frac{\partial}{\partial z}\right)\right] \tag{3.2}$$

and the mean curvature is

$$\mathscr{H} = \frac{1}{q} - \frac{\partial}{\partial z}\left(\frac{r r_z}{q}\right) + \frac{r_\theta^2}{q^3} - \frac{1}{r^2}\frac{\partial}{\partial \theta}\left(\frac{r r_\theta}{q}\right) \tag{3.3}$$

For the case of axisymmetric surfaces, $r = r(z, t)$, (3.1)–(3.3) reduces to

$$\frac{\partial r}{\partial t} = \frac{1}{r}\frac{\partial}{\partial z}\left[\frac{r}{\sqrt{1+r_z^2}}\frac{\partial}{\partial z}\mathscr{H}\right], \qquad \text{(ASDE)} \tag{3.4}$$

where the mean curvature, $\mathscr{H}$, is the sum of the azimuthal principal curvature κ_1 and the axial principal curvature κ_2:

$$\mathscr{H} = \kappa_1 + \kappa_2, \qquad \kappa_1 = \frac{1}{r\sqrt{1+r_z^2}}, \qquad \kappa_2 = -\frac{r_{zz}}{(1+r_z^2)^{3/2}} \tag{3.5}$$

Recall from Section 2 that equilibria are surfaces of constant mean curvature. In cylindrical coordinates the surface of the sphere is $r = \sqrt{\bar{r}^2 - z^2}$, while the cylinder is trivially $r = \bar{r}$. The Delaunay unduloids, $r = r_u(z)$, are more general solutions of the axisymmetric constant mean curvature equation:

$$\frac{1}{r r_z}\frac{d}{dz}\left(\frac{r}{\sqrt{1+r_z^2}}\right) = \mathscr{H}_0 \tag{3.6}$$

where the left hand side of (3.6) is an equivalent form of the curvature in (3.5). Equation (3.6) is scale invariant under $(r, z, \mathscr{H}_0 \to ar, az, \mathscr{H}_0/a)$ and translation invariant, $z \to z + b$, hence without loss of generality, we can

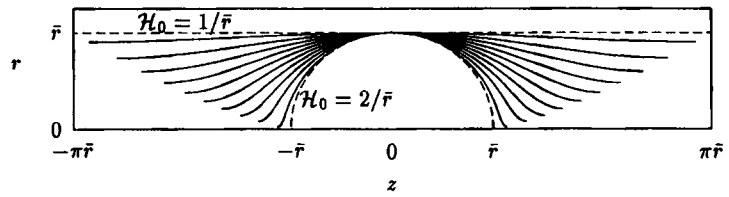

Fig. 2. The family of unduloid arcs with limiting cylinder and sphere.

obtain all unduloids by imposing the initial conditions $r(0) = \bar{r}$, $r_z(0) = 0$ over a range of values for $\mathcal{H}_0$. Note that the cylinder $r(z) \equiv \bar{z}$ is recovered as a solution of (3.6) for $\mathcal{H}_0 = 1/\bar{r}$ and the sphere of radius $\bar{r}$ is obtained in the limit that $\mathcal{H}_0 \to 2/\bar{r}$ (see Fig. 2). The unduloids are a continuous family of intermediate solutions for $1/\bar{r} \leqslant \mathcal{H}_0 \leqslant 2/\bar{r}$.

3.1. Linear Stability of Equilibria

In Section 2.3 we showed that the linearization of surface diffusion about a steady state is

$$\frac{\partial \gamma}{\partial t} = \mathscr{L}\gamma \equiv -\nabla_s^2(\nabla_s^2 + \kappa_1^2 + \kappa_2^2)\,\gamma \tag{3.7}$$

The linear operator $\mathscr{L}$ is self-adjoint with respect to the H^{-1} inner product so all of its eigenvalues are purely real. In Section 2.4 we showed that the stability of surface diffusion equilibria can be computed directly by solving the capillary minimization problem [Vog87, Vog89]. We now review the analytic calculation of the spectrum of the linearized operator for the sphere and cylinder solutions [NM65a, NM65b]. This calculation exploits the fact that the two principal curvatures, κ_1 and κ_2, are constant. We then numerically compute the stability of the unduloid, showing that, as the unduloid approaches the cylinder, the most unstable eigenvalue tends towards zero, while as it approach the sphere, this eigenvalue blows up.

Consider a general infinitesimal perturbation of the form $r(z, \theta, t) \sim r(z) + \varepsilon \hat{r}(z, \theta)\, e^{\lambda t}$. Then the perturbation in the normal direction to the surface is $\varepsilon \hat{r}(z, \theta)\, e^{\lambda t}/\sqrt{1 + r_z^2}$. Thus the eigenvalue problem for (3.7) reduces to

$$\lambda \frac{\hat{r}(z, \theta)}{\sqrt{1 + r_z^2}} = -\nabla_s^2(\nabla_s^2 + \kappa_1^2 + \kappa_2^2)\left(\frac{\hat{r}(z, \theta)}{\sqrt{1 + r_z^2}}\right) \tag{3.8}$$

where the surface Laplacian on $r(z)$ is

$$\nabla_s^2 = \frac{1}{r\sqrt{1+r_z^2}}\left[\frac{\partial}{\partial z}\left(\frac{r}{\sqrt{1+r_z^2}}\frac{\partial}{\partial z}\right)+\frac{\partial}{\partial\theta}\left(\frac{\sqrt{1+r_z^2}}{r}\frac{\partial}{\partial\theta}\right)\right] \tag{3.9}$$

Stability of the Cylinder. Consider the stability of cylinder $r(z)=\bar{r}$, with $\kappa_1 = 1/\bar{r}$ and $\kappa_2 = 0$, to L-periodic perturbations. The Laplacian (3.9) reduces to the constant coefficient operator $\nabla_s^2 = \partial_{zz} + \bar{r}^{-2}\partial_{\theta\theta}$ yielding solutions of (3.8) in terms of the eigenmodes of ∇_s^2 [NM65b],

$$\hat{r}_{n,m}(z) = e^{i2\pi nz/L}e^{im\theta}, \qquad \lambda_{n,m} = -\left(\frac{4n^2\pi^2}{L^2}+\frac{m^2}{\bar{r}^2}\right)\left(\frac{4n^2\pi^2}{L^2}-\frac{1-m^2}{\bar{r}^2}\right) \tag{3.10}$$

for $n, m = 0, 1, 2,\ldots$. Note that the $n = m = 0$ mode corresponds to a change of volume and is excluded by condition (2.13). The $\hat{r}_{0,1}(z)$ mode is neutrally stable and corresponds to translations of the surface perpendicular to the cylindrical axis. More importantly, the $\hat{r}_{1,0}(z)$ mode is long-wave unstable for cylinders with $L > 2\pi\bar{r}$, a result analogous to the well-known Rayleigh instability of liquid jets. All other modes with angular variation, $m > 1$, are linearly stable, strongly suggesting that long-time evolution is dominated by the axisymmetric behavior.

Stability of the Sphere. Similarly, for the sphere $r(z) = \sqrt{\bar{r}^2 - z^2}$, $\kappa_1 = \kappa_2 = 1/\bar{r}$, and the eigenvalue problem reduces to

$$\lambda\sqrt{\bar{r}^2-z^2}\,\hat{r}(z,\theta) = -\nabla_s^2\left(\nabla_s^2+\frac{2}{\bar{r}^2}\right)\left(\sqrt{\bar{r}^2-z^2}\,\hat{r}(z,\theta)\right) \tag{3.11}$$

with the surface Laplacian on the sphere given by

$$\nabla_s^2 = \frac{1}{\bar{r}^2}\frac{\partial}{\partial z}\left((\bar{r}^2-z^2)\frac{\partial}{\partial z}\right)+\frac{1}{\bar{r}^2-z^2}\frac{\partial^2}{\partial\theta^2} \tag{3.12}$$

to yield the eigenmodes in terms of the eigenfunctions of the surface Laplacian, Legendre functions of degree n and order m [Hil76],

$$\hat{r}_{n,m}(z) = \frac{P_n^m(z/\bar{r})}{\sqrt{\bar{r}^2-z^2}}e^{im\theta}, \qquad \lambda_{n,m} = -\frac{n(n+1)(n+2)(n-1)}{\bar{r}^4} < 0 \tag{3.13}$$

corresponding to the results of Nichols and Mullins [NM65b]. Apart from the modes corresponding to changes of volume and translations, all of the eigenmodes are damped, indicating the linear stability of the sphere.

Below we examine the remaining axisymmetric periodic surfaces, the Delaunay unduloids [Del41] and discuss their role in the dynamics of surface diffusion.

Stability of Unduloids. We know from the work of Vogel, [Vog87, Vog89], that the unduloids are unstable. Except for the limiting cases of the cylinder and sphere, unduloids $r_u(z)$ can not be expressed in terms of elementary functions. Indeed, while the sum $\kappa_1 + \kappa_2$ is a constant for the unduloids, $\kappa_1(z), \kappa_2(z)$ both vary in space, further complicating the form of equation (3.8). Consequently we numerically compute the eigenvalues and eigenfunctions of the unduloids via inverse iteration [PTVF92, GvL89]. Given an unduloid with maximum radius $\bar{r}$ (see Fig. 2), there is a single unstable axisymmetric eigenmode with a positive real eigenvalue. The limiting cases of the cylinder, $\mathscr{H}_0 \to 1/\bar{r}$, and the sphere, $\mathscr{H}_0 \to 2/\bar{r}$, are respectively regular and singular limits for the set of unduloids. In the cylinder limit, the unstable eigenvalue approaches zero from above. In the next subsection we show that the unduloids bifurcate subcritically from the cylinder at period $L = 2\pi\bar{r}$, the point where the cylinders change stability. This yields an asymptotic estimate for the unstable eigenvalue in Fig. 3a (shown as a dashed line) in the limit as $\mathscr{H}_0 \to 1/\bar{r}$. In contrast, in the spherical limit, as $2/\bar{r} - \mathscr{H}_0 = \varepsilon \to 0$ the the thickness of the unduloid neck and its width are $\mathcal{O}(\varepsilon)$. Since the eigenfunction is localized to the unduloid neck in this limit, we expect that the unstable eigenvalue $\lambda \sim \mathcal{O}(\varepsilon^{-4})$, for a fourth order linear operator. Via a dashed line, we show that this asymptotic behavior is consistent with the computed values of λ. Note that in the

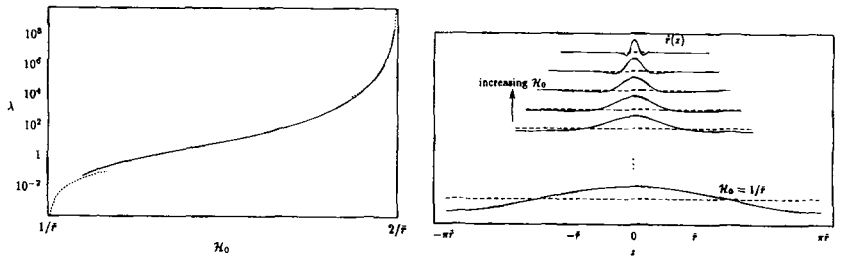

Fig. 3. The unstable eigenmodes for the family of unduloids with curvature $1/\bar{r} \leq \mathscr{H}_0 \leq 2/\bar{r}$, and with minimal radius at $z = 0$. The numerically calculated eigenvalues are shown with the asymptotics for the sphere and cylinder limits (left). The unstable eigenfunction (right) localizes to the neighborhood of the unduloid neck in the sphere limit and approaches a cosine in the cylinder limit.

cylinder limit, the unstable eigenfunction of the unduloid approaches the cosine mode for the cylinder. (See Fig. 3b.)

3.2. Global Dynamics of Axisymmetric Surface Diffusion

In the previous subsection we reviewed the periodic equilibria and their linear stability with respect to periodic perturbations. We now consider the nonlinear dynamics near the periodic equilibria. Coleman *et al.* [CFM95], using higher order perturbation theory, show that despite the fact that cylinders are linearly short-wave stable, the superposition of two perturbations with short periods can lead to nonlinear destabilization of the cylinder and eventual pinchoff. We review one of their specific examples in Section 4.2. Since different periodic equilibria exist with the same volume and period, it is natural to consider the question of their nonlinear stability with respect to perturbations of the same period. Below we use a combination of center-manifold perturbation theory and numerical computations to illustrate that finite amplitude periodic perturbations with period less than 2π can also destabilize the cylinder, leading to finite time pinchoff.

Recall from Section 2.1, the surface diffusion equation conserves the volume of solutions, (2.7),

$$\mathscr{V} = \pi \int_0^L r^2(z)\, dz, \qquad \frac{d\mathscr{V}}{dt} = 0 \tag{3.14}$$

while decreasing their surface area, (2.9),

$$\mathscr{A}(t) = 2\pi \int_0^L r\sqrt{1+r_z^2}\, dz, \qquad \frac{d\mathscr{A}}{dt} = -2\pi \int_0^L \frac{r\mathscr{H}_z^2}{\sqrt{1+r_z^2}}\, dz \leqslant 0 \tag{3.15}$$

Without loss of generality, we consider the family of L-periodic solutions of fixed volume $\mathscr{V} = \pi L$, equal to that of the cylinder with $\bar{r} = 1$. This normalization allows us to compare the relative surface area of the constant mean curvature surfaces enclosing equal volumes. A sphere with volume πL has radius $\bar{r} = (3L/4)^{1/3}$ and surface area $\mathscr{A} = \pi(6L)^{2/3}$ (see Fig. 4). The isolated sphere (shown equivalently as two hemispheres in Fig. 1b) must fit within the interval, $2\bar{r} < L$, hence this surface exists only for periods $L > \sqrt{6}$. For this normalization, the unduloids exist for periods $\sqrt{6} < L < 2\pi$.

Figure 4 shows the surface area of equi-volume constant mean curvature surfaces. The unduloids, where they exist, have the largest surface area of all the constant mean curvature surfaces. For $0 < L < \sqrt{6}$, the cylinder is the only equilibrium and thus is the global minimizer. For

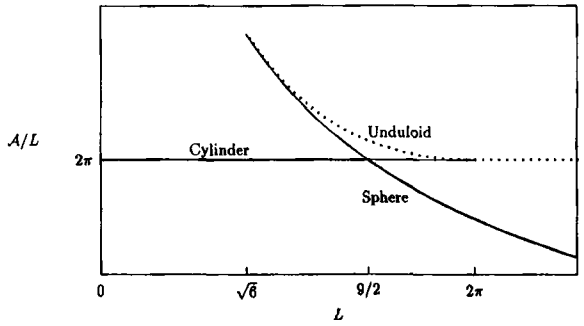

Fig. 4. Surface area over period vs. period for equilibrium states. Those equilibria that are unstable to perturbations of the same period (L) are shown as a dotted line. This includes the branch of unduloids connecting the cylinder to the sphere and the cylinder for $L > 2\pi$.

$\sqrt{6} < L < 9/2$, all three steady states exist with the cylinder as the global minimizer of surface area. For $9/2 < L$, the sphere becomes the global minimizer of surface area. As we showed above, the unduloids are linearly unstable and from (3.15) evolve towards a state with lower surface area. An obvious question is the following: do perturbed unduloids evolve toward the global minimizer of surface area, or can the evolution via surface diffusion tend toward a local minimizer? We address this question next using bifurcation theory.

We begin with a center-manifold expansion [Man90] near the critical period 2π at which the linear stability of the cylinder changes. The conservation of volume for surface evolution introduces an additional constraint on the expansion. This problem bears a strong qualitative similarity to the bifurcation of periodic patterns that arise in solidification (see for example [SB95]). In those problems there is a translation invariance of the front location that corresponds to a conservation law similar to the current volume constraint.

Recall from Section 3.1 that a cylinder of radius $\bar{r} = 1$ becomes linear unstable, on a periodic interval of length L, as L increases through 2π. Expanding the function $r(z)$ as a Fourier series in the neighborhood of the cylinder $\bar{r} = 1$ yields

$$r(z, t) = 1 + \sum_{n=-\infty}^{\infty} A_n(t)\, e^{2\pi i n z/L}, \qquad A_n = A^*_{-n} \tag{3.16}$$

Recall from (3.10) that the $n = 0$ mode is neutrally stable, associated with the conservation of volume. As L increases through 2π the modes with $n = \pm 1$ is become unstable, and the remaining modes are stable. Consequently, there is a two-dimensional center-manifold tangent to $A_{\pm 1}$ at the

origin (that is where $A_n = 0$) and an algebraic constraint associated with volume conservation. Substituting the expansion (3.16) into (3.4) and performing a Galerkin expansion reduces the PDE to an infinite set of coupled ODEs.

Volume conservation, Parseval's theorem, and the expansion (3.16) gives

$$\mathcal{V}_0 = \pi L = \pi \int_0^L r^2 \, dz = \pi L \left((1 + A_0)^2 + \sum_{n=-\infty}^{\infty} |A_n|^2 \right) \tag{3.17}$$

an algebraic constraint determining the neutral constant mode A_0 in terms of the remaining Fourier coefficients.

Proceeding with the center-manifold expansion, we expand the amplitudes of the stable modes (A_k with $|k| > 1$) in terms of the center modes ($A_{\pm 1}$),

$$A_2 = -\tfrac{1}{2}(A_1)^2 + \mathcal{O}(|A_1|^4) \qquad A_k = \mathcal{O}(|A_1|^k) \qquad \text{for} \quad |k| > 1 \tag{3.18}$$

From the volume constraint (3.17), we can solve for A_0

$$A_0 = -|A_1|^2 + \mathcal{O}(|A_1|^4) \tag{3.19}$$

Finally, projecting (3.4) onto the center-manifold and substituting for A_0 and A_2 from (3.19) and (3.18) respectively yields a cubic Landau equation for the amplitude A_1

$$\frac{dA_1}{dt} = -\frac{1}{\pi}(2\pi - L)\, A_1 + 6A_1 |A_1|^2 + \mathcal{O}(A_1 |A_1|^4) \tag{3.20}$$

valid in a small neighborhood of $L = 2\pi$ and $|A_k| \ll 1$.

This equation describes a sub-critical pitchfork bifurcation from the cylinder to a branch of unstable periodic equilibria for $L < 2\pi$ that we identify as the unduloids. The solution on the bifurcating branch has

$$|A_1| = A_u + \mathcal{O}((2\pi - L)^{3/2}), \qquad A_u \equiv \sqrt{\frac{2\pi - L}{6\pi}} \qquad 1 \gg 2\pi - L > 0 \tag{3.21}$$

where the phase of A_1 is arbitrary, reflecting the translational invariance. This becomes apparent if we write the solution for $r(z)$,

$$r \sim \tilde{r}_u(z) = 1 + 2A_u \cos(2\pi(z - z_0)/L) - A_u^2[1 + \cos(4\pi(z - z_0)/L)] + \mathcal{O}(A_u^3) \tag{3.22}$$

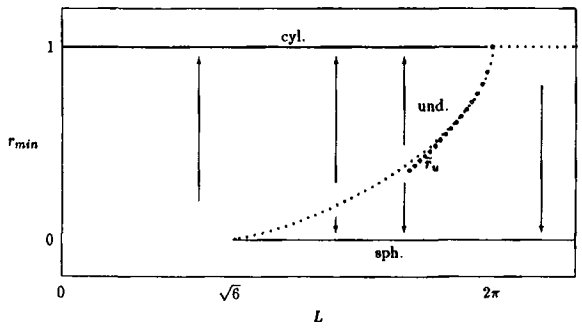

Fig. 5. Bifurcation diagram for the dynamics near the equilibrium surfaces. The solution branches are represented by the minimum value of the radius achieved on the interval $0 \leqslant z \leqslant L$, $r_{\min}$. The results of the center-manifold expansion expansion (3.22) $\tilde{r}_u$ are also plotted for $L \to 2\pi$.

where z_0 is an arbitrary constant related to the phase of A_1. Figure 5 shows that (3.22) matches the unduloid solutions very well as $L \to 2\pi$.

We expect from this bifurcation structure that the stable manifold of the unduloid is a separatrix in phase space that divides the basin of attraction of the cylinder from those solutions that eventually pinchoff, attempting to approach the lower energy spherical solution. The dynamics is shown schematically by the arrows in Fig. 5. In particular, this suggests that for any perturbed unduloid $\tilde{r}$, the sign of the quantity

$$\tilde{\varepsilon} = \left\langle \frac{\tilde{r}(z,t) - r_u(z)}{\sqrt{1 + r_u'^2}}, \hat{r}(z) \right\rangle_{H^{-1}} \tag{3.23}$$

the H^{-1} projection of the perturbation onto the unstable eigenmode, determines the ensuing dynamics.

We performed a numerical study via periodic simulations of the PDE (3.4) to test this conjecture. For ease of computation, we choose a volume preserving perturbation of the unduloid either "toward" or "away" from the cylinder

$$\tilde{r}(z) = \sqrt{(1-\varepsilon)\, r_u(z)^2 + \varepsilon} \tag{3.24}$$

where $\varepsilon = 0$ is the unperturbed unduloid and $\varepsilon = 1$ is the unit cylinder. Positive values of ε perturb "toward" the cylinder while negative values perturb "away" from the cylinder. Our numerical computations of Eq. (3.4) with initial data given by (3.24) indeed verify our description of the separatrix nature of the unduloids. Figure 6a shows a typical solution with

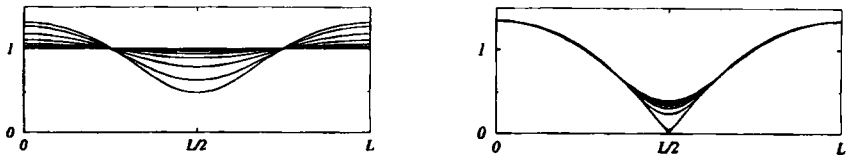

Fig. 6. Evolution of the perturbed unduloid starting with initial data (3.24). In the first case, $\varepsilon = 0.05$ and the perturbation is "towards" the cylinder; we observe relaxation to it in infinite time. In the second case, $\varepsilon = -0.05$ the perturbation is "away" from the cylinder and we observe finite time pinchoff. This particular example is for the unduloid with period $L \approx 5.2 < 2\pi$ however the same qualitative results were seen for all perturbed unduloids.

$\varepsilon > 0$ 0 relaxing back to the cylinder while conversely a very similar solution with $\varepsilon < 0$ (see Fig. 6b) is driven toward pinchoff. Note that these results indicate that finite amplitude periodic perturbations of the cylinder with period less than 2π can destabilize the cylinder to evolve into a finite time pinchoff.

This local description of solution space applies to solutions with low surface areas. In general, there are multiple co-existing separatrices dividing regions in phase space. For example, period n unduloid solutions exist for any interval with $2\pi n > L > n\sqrt{6}$. However, these higher mode solutions have surface area that scale like $\mathcal{O}(n^{1/3})$ and are energetically unfavorable compared with the fundamental solutions described earlier.

Physically, perhaps the most relevant problem is the evolution of a perturbed long (effectively infinite) cylinder. The work of Coleman, Falk, and Moakhar [CFM95, CFM96] shows how the nonlinear interaction of short-wave perturbations can seed the growth of the long-wave instability. Consequently we believe that small-scale imperfections (surface roughness) will eventually drive the surface to pinchoff, even if the scale of the roughness is well below the cylinder radius.

In the following sections we focus on the solutions that are driven to pinchoff. In particular we use numerical computations and asymptotic analysis to describe the self-similar behavior leading up to the time-finite pinchoff singularity.

4. SELF-SIMILAR SOLUTIONS FOR AXISYMMETRIC PINCHOFF

In Section 2 we introduced the equations of motion (3.4) for an axisymmetric surface under the dynamics of surface diffusion,

$$\frac{\partial r}{\partial t} = \frac{1}{r}\frac{\partial}{\partial z}\left(\frac{r}{\sqrt{1+r_z^2}}\frac{\partial}{\partial z}\left(\frac{1}{r\sqrt{1+r_z^2}} - \frac{r_{zz}}{(1+r_z^2)^{3/2}}\right)\right) \tag{4.1}$$

In Section 3 we showed some numerical computations illustrating that certain perturbations of the unduloid (in particular those "away" from the cylinder) can lead to finite time pinchoff. Previous numerical computations of the unstable cylinder [CFM96, CFM95] also indicate a finite time pinchoff. The numerical simulations in [CFM95, CFM96] show that the initial pinchoff results in a change in topology of the surface, with the eventual relaxation to uniform spheres.

When no small length-scales exist in a problem, one might expect the local dynamics of the pinchoff to be self-similar [Bar96]. The problem of self-similarity of pinchoff in free boundary problems has been the subject of much study during the past decade. Examples include both longwave stable problems, such as pinchoff of a thin-neck in the unforced Hele-Shaw cell [ABB96] and rupture of a liquid thin film [BBDK94], and long-wave unstable problems, such as inviscid capillary breakup of a film bridge [CS97], the gravity driven Hele-Shaw cell [GPS93], and droplet pinchoff [Egg93].

In all of these problems the local structure of the pinchoff takes the form

$$r(z, t) \sim \tau^{\alpha} \bar{R}\left(\frac{z - z_c}{\tau^{\beta}}\right)$$

where $\tau = (t_c - t)$ and the exponents α and β suggest that the characteristic scales in the problem go to zero as some power law in $t \to t_c$, where t_c is the time of the pinchoff. Following ideas used in previous studies of self-similar pinchoff, we examine the possibility of such behavior in the surface diffusion problem. In this section we show that there exists a discrete countable family of similarity solutions describing pinchoff, each with a different cone angle. Furthermore, we show that the similarity solution with the largest cone angle is in excellent agreement with the asymptotic behavior of the pinchoff resulting from destabilizing one of the unstable steady solutions described above. In the next section we analyze the stability of these profiles, showing that there is a unique stable one, possessing the largest cone angle, and observed in computations. The fact that we find multiple similarity solutions is not surprising. An analogous phenomena is known for the droplet pinchoff problem [BLS96] where, for the problem with inertia, there are a countably infinite number of similarity solutions, all with the same axial and radial scaling.

Suppose that the axisymmetric solution has a finite time pinchoff singularity at the position $z = z_c$ and at the time $t = t_c$. Actual computation of the pinchoff location and time is a delicate matter that we discuss in more detail at the end of this section. To describe the local behavior near

the pinchoff point and close to the pinchoff time, consider a change of variables in (4.1) to the similarity variables

$$\eta = (z - z_c)/\tau^{\beta}, \qquad s = -\ln(\tau), \qquad \tau = t_c - t \tag{4.2}$$

The time change of variables $s = -\ln(\tau)$ maps finite time behavior in t to infinite time behavior in s. This change allows us, in the next section, to study the linear stability of the self-similar pinchoff profile. We express the similarity solution as

$$r(z, t) = \tau^{\alpha} R(\eta, s).$$

Making the change of variables (4.2) yields the following equation for R in terms of η and τ:

$$\tau^{\alpha-1}(R_s + \beta\eta R_\eta - \alpha R) = \tau^{-2\beta} \frac{1}{R}\left[\frac{R}{Q}\left(\tau^{-\alpha}\frac{1}{RQ} - \tau^{\alpha-2\beta}\frac{R_{\eta\eta}}{Q^3}\right)_\eta\right]_\eta \tag{4.3}$$

where

$$Q = \sqrt{1 + \tau^{2(\alpha-\beta)} R_\eta^2} \tag{4.4}$$

An exact similarity solution of (4.1) corresponds to an s-independent solution of (4.3). The balance of the time dependences on the right hand side of (4.3) and in (4.4) demands that $\alpha = \beta$. Then balancing the time dependences on the left and right hand sides of (4.3) gives $(1/4) = \alpha = \beta$. This is an example of "first type" similarity scaling, where the time dependences can be computed using dimensional analysis [Bar96]. A similarity solution $R(\eta, s) = \bar{R}(\eta)$ satisfies the similarity ODE

$$\frac{1}{4}(\eta\bar{R}_\eta - \bar{R}) = \frac{1}{\bar{R}}\left(\frac{\bar{R}}{\sqrt{1+\bar{R}_\eta^2}}\left(\frac{1}{\bar{R}\sqrt{1+\bar{R}_\eta^2}} - \frac{\bar{R}_{\eta\eta}}{(1+\bar{R}_\eta^2)^{3/2}}\right)_\eta\right)_\eta \tag{4.5}$$

The next subsection analyzes the similarity ODE and its solutions.

4.1. The Similarity ODE: Asymptotics and Computations of Solutions

Pinchoff is a localized phenomenon involving decreasing length-scales and vanishing transport of mass. Consequently, away from the pinch-point z_c, the similarity solution, in original z, t variables, is to leading order time independent as $t \to t_c$. This demands that $\bar{R}$, the solution of (4.5), satisfies

$$\bar{R}(\eta) \sim c_{\pm}\eta, \qquad \eta \to \pm\infty \tag{4.6}$$

Furthermore, since the similarly solution describes the local structure of a tube before pinchoff,

$$\bar{R} > 0 \qquad \text{so that} \quad \pm c_{\pm} > 0 \tag{4.7}$$

Is there a unique solution, many solutions or no solutions to (4.5) satisfying conditions (4.6) and (4.7)? we address this question via asymptotic methods and numerical computations in the following subsections.

A far-field linearization of (4.5) gives us a first indication of the behavior of solutions to the similarity ODE (4.5). Consider a perturbation of a solution that satisfies condition (4.6) in the far-field: $\bar{R}(\eta) \sim c_{\pm}\eta + w_{\pm}(\eta)$ as $\eta \to \pm\infty$. Applying WKB theory [BO78] yields an algebraic solution $w_0(\eta) \sim \eta$, corresponding to a change of far-field slope, and three exponential modes,

$$w_m(\eta) \sim |\eta|^{-5/3} \exp(\tfrac{3}{4}\alpha_m[\tfrac{1}{4}(1+c^2)^2\eta^4]^{1/3}), \qquad m = 1, 2, 3 \tag{4.8}$$

with $\alpha_1 = -1$, $\alpha_{2,3} = (1 \pm i\sqrt{3})/2$. Modes $m = 2, 3$ exhibit exponential growth for large $|\eta|$ and must be suppressed to obtain behavior (4.6). This fixes two boundary conditions at each of the limits $\eta \to \pm\infty$, which suggests, since (4.5) is fourth-order, that the solutions are discrete and locally unique.

4.1.1. Numerical Computations of the Similarity Profiles. We conducted a numerical search for solutions to (4.5) using a finite difference approximation of (4.5) on a suitably large finite domain and a Newton–Raphson relaxation method for finding solutions. The computations were done on a finite but suitably large domain. The far field conditions (4.6) were satisfied by imposing $\eta\bar{R}_\eta - \bar{R} = 0$ (an eikonal approximation of Eq. (4.5)) at the end points and at the second to last end points, thus giving "four" boundary conditions for a fourth-order equation. In terms of the WKB expansion (4.8), the asymptotic boundary conditions suppress the exponentially growing modes and yield locally unique solutions of (4.5).

As the starting point for the iterative method we use an exact solution of the long-wave approximation, described below, with prescribed far-field slopes $c_{\pm}$; regardless of the choice of far-field slopes or symmetry of the guess, the Newton–Raphson iteration always rapidly converged to a symmetric similarity solution with a nearby slope. Using this method, we found the symmetric solutions, $\bar{R}_i(\eta)$, $i = 0, 1, 2, \ldots$, a countably infinite set ordered by the far field slope $c_0 > c_1 > c_2 > \cdots$. Figure 7 shows a plot of the first ten similarity solutions. Table I lists the center value $\bar{R}_i(0)$, the far field slopes, $c_i = \bar{R}_i'(\infty)$, and the half cone angles, $\phi_i = \tan^{-1}(c_i)$, for the first six similarity solutions.

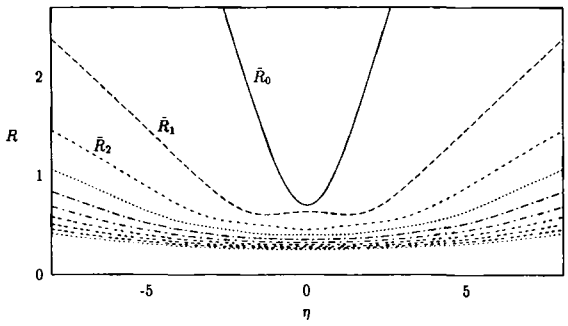

Fig. 7. First ten similarity solutions, $\bar{R}_i(\eta)$, $i = 0, 1, 2, \ldots, 9$.

We note that even though the iterative scheme used strongly non-symmetric initial guesses, it always converged to a symmetric solution $\bar{R}(\eta)$. We conjecture that the only solutions of (4.5) satisfying (4.6)–(4.7) are the countable set of symmetric solutions described here.

Since the numerically computed far field slopes c_i go to zero as $i \to \infty$, we compare the computed solutions with corresponding exact solutions of a long-wave approximation described below.

4.1.2. The Long-Wave Approximation of the Similarity ODE.

We can simplify Eq. (4.5) via a small cone-angle approximation. Consider the rescaling

$$R = \varepsilon \tilde{R}(\tilde{\eta}), \qquad \eta = \frac{\tilde{\eta}}{\varepsilon} \tag{4.9}$$

for $0 < \varepsilon \ll 1$. This scaling yields $R_\eta = O(\varepsilon^2)$, $\sqrt{1 + R_\eta^2} \sim 1 + O(\varepsilon^4)$, and the equation for the steady similarity solution reduces to

$$\frac{1}{4}(\tilde{\eta}\tilde{R}_{\tilde{\eta}} - \tilde{R}) = \frac{1}{\tilde{R}}\left(\tilde{R}\left(\frac{1}{\tilde{R}}\right)_{\tilde{\eta}}\right)_{\tilde{\eta}} + O(\varepsilon^4) \tag{4.10}$$

Table I

i	$\bar{R}_i(0)$	c_i	ϕ_i
0	0.701595	1.03714	46.0444°
1	0.636461	0.29866	16.6288°
2	0.456842	0.18384	10.4170°
3	0.404477	0.13489	7.68279°
4	0.355884	0.10730	6.12470°
5	0.326889	0.08942	5.11027°

Equation (4.10) is scale invariant under the transformation (4.9) for any $\varepsilon > 0$; as a result, it reduces to a phase plane system in terms of the variables

$$U(\zeta) = \tilde{\eta}\tilde{R}, \qquad V(\zeta) = \tilde{\eta}(\tilde{R} + \tilde{\eta}\tilde{R}_{\tilde{\eta}}), \qquad \zeta = \ln|\tilde{\eta}| \tag{4.11}$$

to yield the autonomous system

$$\frac{dU}{d\zeta} = V, \qquad \frac{dV}{d\zeta} = \frac{1}{2}U^2\left(U - \frac{1}{2}V\right) + V + \frac{V^2}{U} - U \tag{4.12}$$

This representation shows that Eq. (4.10) has a continuous one-parameter family of solutions, parametrized by the ratio $\mu = c_+/c_-$, with the appropriate limiting behavior as $\tilde{\eta} \to \infty$ (see Fig. 8). Of these solutions there is a unique symmetric solution (see Fig. 8). In addition to offering some insight on the asymptotic form of (4.3), this long wave approximation was used to generate initial guesses for the Newton–Raphson iteration method for the full similarity ODE (4.5).

Equation (4.10) is a uniform approximation of (4.5) to $O(\varepsilon^4)$. If we choose ε to be equal to the square root of the far-field slope, $\varepsilon = \sqrt{c_i}$, then the full solution to the similarity ODE and its long-wave approximant have identical leading order far-field behavior. Consequently, we can express each similarity solution in terms of the long wave theory and a deviation,

$$\bar{R}(\eta) = \sqrt{c_i}\,\tilde{R}_0(\sqrt{c_i}\,\eta) + c_i^2 W_i(\sqrt{c_i}\,\eta) \tag{4.13}$$

where $\tilde{R}_0(\tilde{\eta})$ is the unique symmetric solution of (4.10) with $\tilde{R}_0'(\tilde{\eta} \to \infty) \to 1$. As shown in Fig. 9, the deviation is $O(\varepsilon^4)$ with a finite amplitude smooth

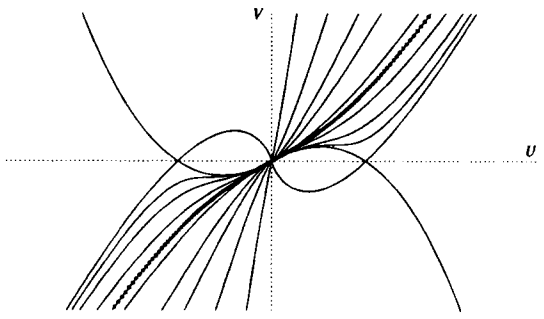

Fig. 8. $U - V$ phase plane for the long wave Eq. (4.10). Shown are various solutions all with the appropriate far field asymptotic behavior to describe conical pinchoff. The symmetric solution is drawn with a heavy dotted line.

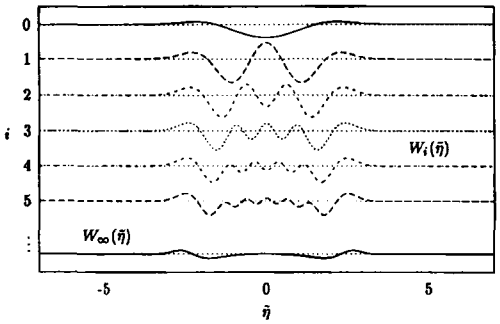

Fig. 9. Leading order long-wave deviation $W_i(\eta)$ for the first six similarity solutions and the limiting behavior.

limiting profile $W_i(\tilde{\eta})$ as $i \to \infty$. Note that since the far field of the long-wave solution satisfies (4.6), W_i must have the asymptotic behavior as the WKB results given earlier. Figure 9 shows that the first order deviations $W_i(\tilde{\eta})$ are localized to a neighborhood of the origin and validate the long wave approximation (see Fig. 9). As the index i increase $W_i(\tilde{\eta})$ develops more oscillations, and $W_i(\tilde{\eta})$ has $2(i+1)$ nodes. These oscillations are due to higher-order near-field effects and decrease in amplitude as $c_i \to 0$. Note that substituting (4.13) into Eq. (4.5) for finite values of c_i yields a nonlinear problem of the form

$$\mathcal{G}(W_i(\tilde{\eta}); c_i) = 0 \tag{4.14}$$

that would yield the values c_i as discrete eigenvalues and the deviations $W_i(\tilde{\eta})$ as bounded oscillatory modes with far field exponential decay.

4.2. Evidence of Self-Similarity in Numerical Computations of Pinchoff

The numerical and asymptotic results of the previous subsection suggest the existence of a countably infinite, discrete set of symmetric similarity solution describing pinchoff of an axisymmetric tube under the motion of surface diffusion. In this section we perform numerical computations of Eq. (4.1) using self-similar adaptive mesh refinement to capture the structure of the pinchoff. Our goal here is to determine numerically which of the symmetric similarity solutions are actually observed in the pinchoff process. The details of the numerical scheme are presented in the appendix.

First we show a calculation using the initial data from the first numerical computation presented in [CFM95] (see Eq. (57) in that paper). This

choice of initial data is symmetric about the eventual pinch-point and we exploit the symmetry in our computation. In a second calculation we choose initial data for which the interface closely approximates an array of spheres joined together by thin filaments (string of pearls). In this case the solution is not symmetric about the pinch point. In both cases, regardless of the symmetry of the initial condition, the local structure of the pinchoff showed excellent agreement with that of the symmetric similarity solution $\bar{R}_0$, shown in Fig. 7.

Case 1: CFM Initial Data. The initial data is

$$r(z, 0) = 1 + 0.05[\cos(11z/2) + \cos(5z)] \tag{4.15}$$

This initial condition has a minimum period of 4π and is symmetric about $z = 0$. We exploit this symmetry to compute on the half interval from 0 to 2π.

We initially chose this data as a first test of our code, since we use a different scheme from that used in [CFM95]. At early and intermediate times our results showed excellent agreement with those in [CFM95].

Then we compare our simulation at times close to the singularity time with the similarity solution. Using a self-similar adaptive mesh refinement scheme we resolved the singularity to very small length-scales. The solution develops a finite time pinchoff at the origin, with a local cone angle equal to that of the similarity solution $\bar{R}_0$. Profiles of the solution are shown in Fig. 10 at times close to the pinchoff time, which we measure to be at roughly $t = 30$. Precise determination of the pinchoff time for an initial value problem is difficult due to the accumulation of discretization and round-off error that occurs in any discrete time-stepping scheme. However we can more precisely compute the time to pinch, and those values are given in the caption of Fig. 10.

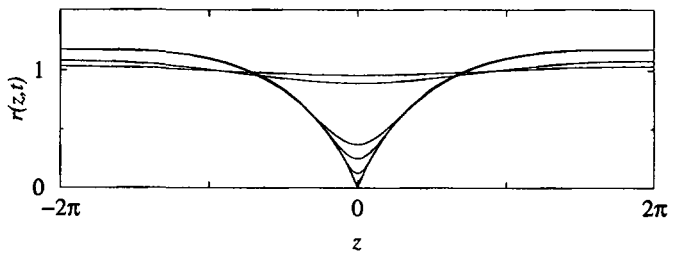

Fig. 10. The evolution of the interface from initial data (4.15). The solution pinches in a symmetric fashion with a fixed cone angle equal to that of the similarity solution $\bar{R}_0$. Shown are profiles of $r(z, t)$ with respective numerical values of the time to pinchoff, $\tau = t_c - t$, equal to 10, 5, 8.7×10^{-2}, 1.7×10^{-2}, 1.1×10^{-3}, 6.5×10^{-5}, 2.0×10^{-6}, and 2.6×10^{-7}.

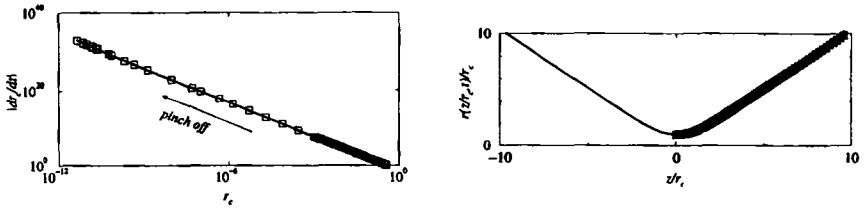

Fig. 11. (a) Validation of the time dependence of r_c. A graph of r_c vs. $|dr_c/dt|$ comparing the numerical data (□) with the similarity solution (black line), $|dr_c/dt| = \bar{R}_0(0)^4/(4r_c^3)$. There are no free parameters in the fit. (b) Rescaled height profiles over eight orders of magnitude in the pinchoff radius. Profiles obtained from the PDE simulation are plotted with various symbols corresponding to the value of r_c; for $r_c = 2.4 \times 10^{-2}$, □ for $r_c = 7.5 \times 10^{-4}$, ◇ for $r_c = 2.3 \times 10^{-5}$, △ for $r_c = 7.0 \times 10^{-7}$, ◁ for $r_c = 2.1 \times 10^{-3}$, and * for $r_c = 6.4 \times 10^{-10}$. All of the data collapse directly onto the similarity profile $\bar{R}_0$, shown with a solid bold black line.

From the similarity variables (4.2) with $\alpha = \beta = (1/4)$, we anticipate that the characteristic width of the pinch region scales like the radius at the pinchoff position $r_c(t) = r(z_c, t)$. We verify that the time dependence of r_c is consistent with the similarity solution. Since the actual critical time is difficult to compute due to accumulated errors, we compare with "dynamic" measure of r_c by plotting it against the numerical value of its time derivative. Figure 11a shows r_c vs. $|dr_c/dt|$. The boxes (□) show the numerical data while the soled line is a graph of the curve $|dr_c/dt| = 0.060575684/r_c^3$, satisfied by the similarity solution $\bar{R}_0$, where $\bar{R}_0(0)^4/4 = 0.060575684$. Notice that the agreement is excellent. This confirms the time dependence of the minimum height with *no free parameters* in the fit. We now compare the local structure of the pinch to the similarity solutions found in the previous subsection. Since we can easily compute r_c numerically, we rescale the $r(z, t)$ plots near the pinch point by dividing the space variable z and the height by r_c. Figure 11b shows this data compared to the similarity solution R_0 rescaled in the same fashion. There is excellent agreement with the similarity profile and complete collapse of the data in the similarity coordinates.

Case 2: String of Pearls. The initial data is

$$r(z) = \begin{cases} \delta + \sqrt{25 - z^2}\, e^{-\gamma/(1 - z^2/25)^2}, & |z| \leqslant 5, \\ \delta, & 5 < |z| < 10 \end{cases} \tag{4.16}$$

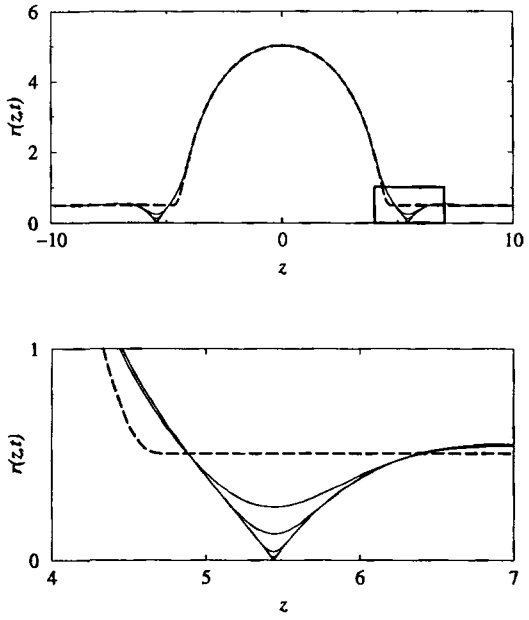

Fig. 12. Evolution of the interface starting with "string of pearls" initial data (4.16) shown above as the dashed line. The solution pinches in two points on either side of the sphere. Locally near the pinchoff we blow up the box in the second figure to show that the structure of the pinchoff is again symmetric.

on $[-10, 10]$ with periodic boundary conditions at the endpoints. For the computation presented here, we chose $\delta = \frac{1}{2}$ and $\gamma = 0.1$.

Figure 12 shows the solution as it starts to pinch. The "spherical" region stays roughly spherical while the solution pinches near the end of the sphere. This is expected since the initial data has constant curvature in the spherical region The solution is not symmetric about the point of pinch yet the local structure of the pinch is again consistent with the symmetric similarity solution $\bar{R}_0$.

5. STABILITY OF SIMILARITY PINCHOFF PROFILES

In the previous section we examined the possible forms for self-similar pinchoff behavior in axisymmetric motion by surface diffusion. In this section we develop a stability theory that explains why a particular solution is dynamically selected.

Recall that in axisymmetric coordinates, the equation of motion is

$$\frac{\partial r}{\partial t}=\frac{1}{r}\frac{\partial}{\partial z}\left[\frac{r}{\sqrt{1+r_z^2}}\frac{\partial}{\partial z}\left(\frac{1}{r\sqrt{1+r_z^2}}-\frac{r_{zz}}{(1+r_z^2)^{3/2}}\right)\right] \tag{5.1}$$

For a self-similar pinchoff at a point z_c we look for a solution to (5.1) in which $r(z_c, t)\to 0$ at a finite time t_c. Via a careful numerical study, we found a countably infinite set of symmetric similarity solutions $\bar{R}_i(n)$, $i=0, 1, 2$, each describing a possible path to axisymmetric pinchoff. Each of these similarity solutions describes pinchoff in which the interface locally approaches a cone on each side of the pinch point z_c. All of the similarity solutions are symmetric about the pinch-point z_c, yielding the same far-field cone angle on either side of z_c.

Despite the fact the we found many similarity solutions, the only one ever observed to describe the local structure of the pinchoff, in numerical computations of the PDE, is similarity solution $\bar{R}_0$. In Section 4.2, we presented an example of a refined numerical computation of such a pinchoff and compared the local structure with the similarity solution $\bar{R}_0$. We found beautiful agreement over many decades of scaling in the minimum as pinchoff is approached.

In this section we show that the reason the smaller cone angle similarity solutions $\bar{R}_1, \bar{R}_2,\ldots$ are never observed in pinchoff is that they are all linearly unstable to small perturbations. Hence, generically they will not occur in a pinchoff calculation. Section 5.1 presents the detailed linear stability analysis, in similarity variables, of the similarity profiles $\bar{R}_i$. Part of the difficulty of studying linear stability of a similarity solution is that the transformation to similarity variables requires understanding how symmetries, of the original unrescaled PDE, transform. We show that for the axisymmetric problem, time translation and space translation, expressed in similarity variables, lead to two anomalous positive eigenvalues in the spectrum of the linearized operator. If the remainder of the eigenvalues are negative, then modulo translations in time and space (invariances of the original PDE), the similarity solution is linearly stable. In Section 5.1.2 we numerically compute all the positive eigenvalues of the linearization about the similarity solution $\bar{R}_i$ and show that except for the solution $\bar{R}_0$, all of $\bar{R}_i$ have positive eigenvalues associated with instability.

In Section 5.2 we present a numerical computation illustrating the instability of the similarity solutions $\bar{R}_1$. We show that the destabilization of the solution is in excellent agreement with the linear stability analysis described below. Finally in 5.3 we examine the stability of the axisymmetric similarity solutions with respect to non-axisymmetric perturbations. We show there that the similarity solution $\bar{R}_0$ is also stable to non-axisymmetric

perturbations, making it an excellent candidate for generically describing pinchoff of a non-axisymmetric tube.

5.1. Linear Stability Analysis

In order to understand the linear stability of the similarity solution, we work in similarity variables. Making a change of variables in Eq. (5.1) to similarity variables

$$\eta = (z - z_c)/\tau^{1/4}, \qquad r = \tau^{1/4} R(\eta, s), \qquad s = -\ln(\tau), \qquad \tau = t_c - t \tag{5.2}$$

yields the similarity form of the PDE (5.1):

$$R_s + \frac{1}{4}(\eta R_\eta - R) = \frac{1}{R}\left(\frac{R}{\sqrt{1+R_\eta^2}}\left(\frac{1}{R\sqrt{1+R_\eta^2}} - \frac{R_{\eta\eta}}{(1+R_\eta^2)^{3/2}}\right)_\eta\right)_\eta \tag{5.3}$$

The time change of variables $s = -\ln(t_c - t)$ maps finite time behavior in t to infinite time behavior in s.

The similarity solutions $\bar{R}_i$ computed in Section 4.1.1 are "steady" (s-independent) solutions of (5.3). To compute their stability we linearize (5.3) about each of the $\bar{R}_i$. We note that (5.3) can be written in the form

$$R_s = -\tfrac{1}{4}(\eta R_\eta - R) + \mathcal{N}(R) \tag{5.4}$$

where the functional $\mathcal{N}(R)$ is the right-hand side of Eq. (5.3).

Substituting $R(\eta, s) = \bar{R}(\eta) + \varepsilon P(\eta, s)$ and linearizing (5.4) in P yields

$$P_s = \mathcal{L}(\bar{R})\, P, \qquad \mathcal{L}(\bar{R})\, P = -\tfrac{1}{4}(\eta P_\eta - P) + \delta \mathcal{N}(\bar{R})\, P \tag{5.5}$$

the linearization about the steady state $\bar{R}$.

In addition, we need to apply boundary conditions to P in the far-field. Consider a matching regime near the pinchoff region in primitive variables, $|z - z_c| \leqslant 1$, but in the far-field of the pinchoff in similarity variables, $|\eta| = |z - z_c|/\tau^{1/4} \gg 1$. We assume that although rapid changes are taking place on small scales close to pinchoff point, that the evolution in the far-field still occurs on a time-scale of order unity, $r_t \sim \mathcal{O}(1)$. In similarity variables this yields the boundary conditions

$$R_s + \tfrac{1}{4}(\eta R_\eta - R) \to 0 \qquad \text{for} \quad |\eta| \to \infty \tag{5.6}$$

Note that if $\bar{R}$ is linear in the far-field that it satisfies (5.6) and thus the perturbation, P, also satisfies this linear boundary condition. Since (5.6) depends on the rescaled time, s, the associated linear stability eigenproblem

has the eigenvalue appearing in the boundary condition. The boundary conditions provides two constraints at each boundary by eliminating the exponentially growing modes found by WKB theory in the previous section.

5.1.1. Symmetry Modes of Linearized Operator. The linear stability problem derived above (5.5), (5.6) has a discrete spectrum. However, certain modes in the spectrum are associated with the symmetries of the problem. It is well known that linearizing the actions of certain symmetries in physical space can lead to null modes for the linear operator [CH93, WB98]. In our problem, because we are working in similarity variables, *linearizing the symmetries can lead to anomalous positive eigenvalues.* Both time and space translation in the original PDE yield positive eigenvalues in the spectrum of the linear problem (5.5), (5.6). This is because a fixed size ε translation in the space variable $z \to z + \varepsilon$ leads to a dilating translation of the similarity variable $\eta \to \eta + \varepsilon e^{s/4}$. Likewise a translation in the time variable, t, transforms to an exponential dilation of the similarity solution. We first show that linearizing the symmetry operation yields a solution to the linearized problem, and then explicitly derive the eigenvalues and eigenfunctions of $\mathscr{L}$ in (5.5) associated with time and space translation.

Suppose ε parametrizes a continuous symmetry, which transforms a steady solution $\bar{R}(\eta)$ to a family of solutions $\bar{R}(\eta, s; \varepsilon)$ with $\varepsilon = 0$ corresponding to the identity, i.e., $\bar{R}(\eta) = \bar{R}(\eta, s; 0)$. Expanding around $\varepsilon = 0$ yields

$$\bar{R}(\eta, s, \varepsilon) = \bar{R}(\eta) + \varepsilon \bar{R}_\varepsilon + \mathcal{O}(\varepsilon^2) \tag{5.7}$$

where $\bar{R}_\varepsilon$ represents the direction of an infinitesimal application of the symmetry (i.e., an infinitesimal generator of the symmetry),

$$\bar{R}_\varepsilon = \left.\frac{\partial \bar{R}(\eta, s; \varepsilon)}{\partial \varepsilon}\right|_{\varepsilon = 0} \tag{5.8}$$

Substituting (5.7) into the similarity PDE (5.4) and expanding to order ε shows that R_ε satisfies the linearized similarity equation, (5.5),

$$(\bar{R}_\varepsilon)_s = \mathscr{L}(\bar{R})\, \bar{R}_\varepsilon \tag{5.9}$$

Let us now examine the spatial and temporal translation symmetries explicitly.

Consider the *spatial translation symmetry*, $z \to z + \varepsilon$. In terms of similarity variables, this transforms $\eta \to \eta + \varepsilon e^{s/4}$, and to linear order in ε

$$\bar{R}_i(\eta) \to \bar{R}_i(\eta + \varepsilon e^{s/4}) \sim \bar{R}_i(\eta) + \varepsilon \bar{R}_i'(\eta)\, e^{s/4} \tag{5.10}$$

The order ε contribution must satisfy the linearized similarity equation,

$$\mathscr{L}(\bar{R})\,\bar{R}'(\eta) = \tfrac{1}{4}\bar{R}'(\eta),$$

producing the spatial-translational eigenfunction $\bar{R}_{i,Z}(\eta) \equiv \bar{R}_i'(\eta)$ with eigenvalue $\lambda_Z = 1/4$.

Similarly, the *time shift symmetry*, $t \to t + \varepsilon$ takes $\tau \to \tau(1 - \varepsilon e^s)$ and expanding to order ε yields

$$\bar{R}_i(\eta) \to (1-\varepsilon e^s)^{1/4}\,\bar{R}_i(\eta(1-\varepsilon e^s)^{-1/4}) \sim \bar{R}_i(\eta) + \varepsilon\,\tfrac{1}{4}(\eta\bar{R}_i'(\eta) - \bar{R}(\eta))\,e^s,$$

producing the the time-shift eigenfunction $\hat{R}_{i,T}(\eta) = \frac{1}{4}(\eta\bar{R}_i'(\eta) - \bar{R}_i(\eta))$ and eigenvalue $\lambda_T = 1$.

The eigenfunctions corresponding to λ_Z and λ_T and other possible symmetries of the equation are anomalous in the sense that they are not associated with structural instabilities; they correspond to infinitesimal translations in z_c and t_c. They are associated with positive eigenvalues because two pinchoff solutions shifted slightly in space and/or time in physical variables appear to be diverging exponentially in s. If we consider the evolution of a perturbed similarity solution, projections on these modes can be eliminated through small shifts in z_c and t_c, corresponding to a shift of the pinchoff's location in space and time.

If we consider non-axisymmetric perturbations, then four more geometric symmetries are relevant, corresponding to translations and rotations of the solution. We discuss these in Section 5.3.

5.1.2. The Spectrum and Eigenfunctions of the Linearized Operator. The time and space translational symmetry of the PDE gives us two points in the spectrum of $\mathscr{L}$: $\lambda_T = 1$ resulting from time translation and $\lambda_Z = 1/4$ resulting from space translation. To determine the rest of the spectrum of $\mathscr{L}$ and corresponding eigenfunctions, we use numerical methods.

Since $\mathscr{L}$ is the linearization of a nonlinear diffusion operator, we expect the spectrum to have only a finite number of positive eigenvalues and an infinite set of negative modes (a result supported by our numerical calculations). We are interested in which similarity solutions are stable, so we present numerical computations only for the positive eigenvalues associated with the linearized operator $\mathscr{L}$.

We compute each $\bar{R}_i$ numerically using the finite difference Newton–Raphson method outlined in Section 4. The Newton–Raphson scheme yields a discretization of the linear operator $\mathscr{L}(\bar{R}_i)$ in the form of a banded Jacobian matrix. Calculating the eigenmodes of this matrix provides

estimates of the eigenvalues and discretizations of the eigenmodes of the linear operator. We compute the dominant eigenvalues and eigenvectors using a generalized, complex inverse iteration scheme [PTVF92, GvL89]. Each similarity solution $\bar{R}_i$ has a corresponding linear stability operator $\mathscr{L}(\bar{R}_i)$ with $2i+2$ positive modes, including the two that result from time and space translation. All of the positive eigenvalues are purely real (see Fig. 13). We tested the accuracy of this procedure by measuring how well the method recovered the known eigenfunctions and eigenvalues from the symmetry groups.

From Fig. 13 we see that the fundamental solution $\bar{R}_0(\eta)$ is the only similarity solution with no positive eigenvalues apart from the symmetry modes. Each of the successive similarity solutions $\bar{R}_i(\eta)$, $i=1, 2, 3,...$, has two more unstable modes than the previous one. These modes are created in symmetric/anti-symmetric pairs with a separation in the eigenvalues that decreases as i increases.

The far-field asymptotics of the eigenfunctions of the linear operator $\mathscr{L}$ can be derived from examining the far-field time-independent nature of the similarity solutions. As $|\eta| \to \infty$, the algebraic solution satisfying the boundary condition (5.6) behaves as

$$\hat{R}(\eta) \sim |\eta|^{1-4\lambda} \qquad |\eta| \to \infty \tag{5.11}$$

This algebraic decay in the far-field is consistent with the symmetry modes, $\lambda = \frac{1}{4}, 1$. Additionally, from (5.11) we see that any perturbation, with super-linear growth for large $|\eta|$, decays in time.

The linear stability only describes the dynamics near $\eta = 0$; we expect that the eigenfunction expansion only converges in an L^2 norm with a exponentially decaying weight function (see [GK87, FK92, Way97]).

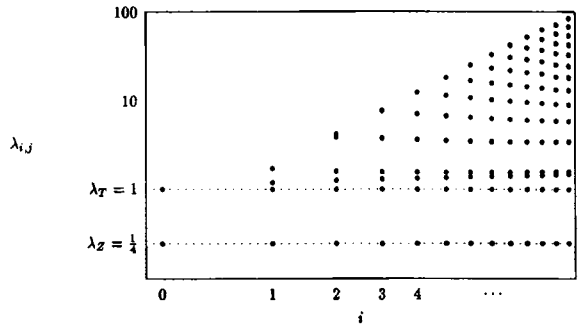

Fig. 13. Positive eigenvalues for the discrete similarity solutions, $\bar{R}_i(\eta)$, $i=0, 1, 2,...$. Note that $\lambda_z = 1/4$ and $\lambda_T = 1$ are anomalous positive eigenvalues associated with space and time translation.

In the next section, we examine the changes of the far-field slope and other global structural changes that arise from the instability of the unstable similarity solutions; the nonlinear nature of these dynamics forces us to examine the problem numerically.

5.2. Comparison with Simulations of the Fully Nonlinear System

We perform computations of the full PDE (5.1) that confirm the linear stability theory predicted above. The computations from Figs. 10 and 11 in Section 4 illustrate that the stable similarity solution $\bar{R}_0$ is recovered over many decades of scaling in the pinching of the solution.

Now we take one of the unstable similarity solutions found in Section 4 and show via direct numerical simulation that this solution is unstable. We consider the first unstable similarity solution $\bar{R}_1(\eta)$, with half-cone angle $\phi_1 = 16.63°$. Linear stability analysis for $\bar{R}_1(\eta)$ yields two unstable modes, apart from the symmetries, with eigenvalues $\lambda_{1,1} = 1.2048$ and $\lambda_{1,0} = 1.7328$ (see Fig. 13). The largest eigenvalue $\lambda_0 = 1.7328$ has a corresponding eigenfunction $\hat{R}_{1,0}(\eta)$ that is antisymmetric while the second eigenvalue $\lambda_1 = 1.2048$ has the symmetric eigenfunction $\hat{R}_{1,1}(\eta)$.

We consider an initially small antisymmetric perturbation of the symmetric similarity solution $\bar{R}_1(\eta)$ and watch how this perturbation grows in a simulation of the fully nonlinear PDE. We show that the initial growth of the perturbation is dominated by the $\hat{R}_{1,0}(\eta)$ eigenmode. Our computation was done on a large finite domain, $[-L, L]$ with $L = 20$, with Neumann boundary conditions consistent with the initial data,

$$r_z = (\pm L) = c_1, \qquad r_{zzz}(\pm L) = 0 \tag{5.12}$$

and initial data

$$r(z, 0) = \bar{R}_1(z) + 0.001 \sin(z)\, e^{-z^2/4} \tag{5.13}$$

The evolution is depicted in Fig. 14.

In the absence of the perturbation term in (5.13), this initial data would yield $\bar{R}_1$ self-similar pinchoff at position $z_c = 0$ and time $t_c = 1$. To numerically separate the antisymmetric perturbation from the evolving solution we compute the antisymmetric part of the solution

$$r_{\text{odd}}(z, t) = \tfrac{1}{2}(r(z, t) - r(-z, t)) \tag{5.14}$$

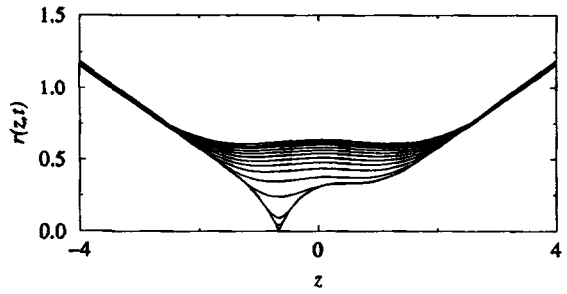

Fig. 14. Destabilization of the unstable similarity solution $\bar{R}_1$ by an antisymmetric perturbation given in (5.13). The eventual pinchoff has local structure of the stable similarity solution $\bar{R}_0$.

In Figs. 15a, b we show that this perturbation does evolve according to the dominant eigenmode, in terms of z, t,

$$\hat{r}_{1,0}(z,t) = (1-t)^{1/4}\,\hat{R}_{1,0}(z/(1-t)^{1/4})\,e^{-\lambda_{1,0}\ln(1-t)} \tag{5.15}$$

In Fig. 15a we compare the amplitude of the perturbation $r_{\text{odd}}(z,t)$ with the evolution predicted by (5.15), namely the power law $(t_c-t)^{1/4-\lambda_{1,0}}$. Note that Fig. 15a is on a log-log scale where the power law is represented by a straight line with slope $1/4-\lambda_{1,0}\approx -1.48$. The comparison with the fully nonlinear simulation (the Δ's) shows extremely good agreement at

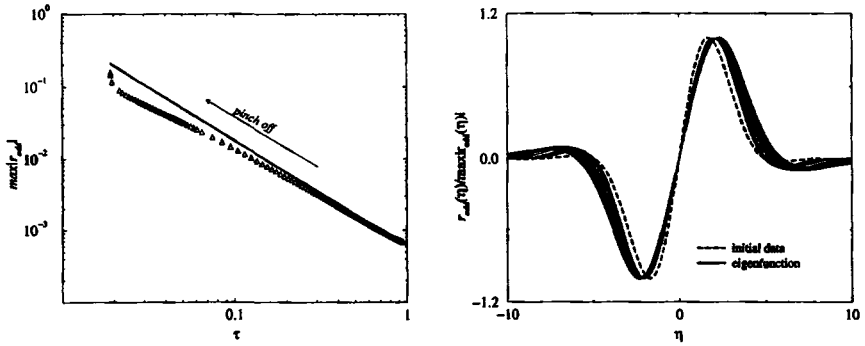

Fig. 15. (a) The amplitude of the perturbation as defined in (5.14) compared with the evolution predicted by linear stability theory, $(t_c-t)^{1/4-\lambda_0}$. The comparison with the fully nonlinear simulation shows extremely good agreement at early times with departure at later times as the nonlinearities in the dynamics become more important. The perturbation profile $r_{\text{odd}}(z,t)$ rescaled in similarity variables evolving in time towards the most unstable eigenfunction $\hat{R}_{1,0}(\eta)$.

early times with departure from linear theory at later times as the nonlinearities in the dynamics become more important. Moreover, in Fig. 15b we show the excellent agreement of the spatial profile of the perturbation $r_{\text{odd}}(z, t)$ with the eigenfunction $\hat{R}_{1,0}(\eta)$ for times from $\tau = t_c - t = 0.9$ to 0.04. During this time, the perturbation has grown by approximately two orders of magnitude. However, as $\tau \to 0$ and pinchoff is approached more complicated nonlinear effects come into play, interacting with the linearized evolution (see Fig. 14). Observe that the perturbation causes one of the local minima of $\bar{R}_1(\eta)$ to become a new pinchoff position z_{new}, with possibly a new critical time t_{new}. This evolution necessarily involves the translation symmetry modes λ_Z and λ_T. As mentioned earlier (5.11), nonlinear effects are necessary to modify the local structure around the pinchoff position to yield the appropriate far field of the stable similarity solution $r \sim (t_{\text{new}} - t)^{1/4} \bar{R}_0((z - z_{\text{new}})/(t_{\text{new}} - t)^{1/4})$. The fact that λ_Z, $\lambda_T > 0$ reflects the sensitivity of the dilational form of the similarity variables (5.2) on the values z_c, t_c.

5.3. Non-Axisymmetric Perturbations

In addition to linear stability of the similarity solutions with respect to axisymmetric perturbations, it is important to consider the possible influence of more general deformations. Unstable modes with angular dependence would cause cylindrical solutions to destabilize, yielding more complicated non-axisymmetric surfaces. Our calculations show that this is not the case.

Consider a non-axisymmetric perturbation of the axisymmetric similarity solution of the form

$$R(\eta, \theta, s) = \bar{R}_i(\eta) + \varepsilon \hat{R}^m_{i,j}(\eta) \cos m(\theta - \theta_0)\, e^{\lambda s} \tag{5.16}$$

where we have exploited the axisymmetry of the base state to decouple the solution into angular modes. Note that the rotational invariance allows θ_0 to be chosen arbitrarily—choosing 0 and $\pi/2$, for example, yields cosines and sines which span the set of angular functions. The stability analysis proceeds by substituting into the full governing Eqs. (3.1)–(3.3) and linearizing about the similarity solution to obtain the eigenvalue problem:

$$\lambda \hat{R}^m_{i,j} = \mathscr{L}^m(\bar{R}_i)\, \hat{R}^m_{i,j} \tag{5.17}$$

The resulting expressions are extremely cumbersome and the MAPLE symbolic manipulation program was used to formulate the analytic problem for the numerical computation of the eigenvalues.

As was described in Section 5.1, the eigenmodes connected to invariant symmetries can be obtained analytically. In addition to the two axisymmetric modes for $m=0$, there are four symmetry modes for $m=1$.

Two of these correspond to translations of the cylindrical axis in the transverse plane and have $\lambda = 1/4$. Consider *spatial translation in* x, $x \to x+\varepsilon$. In terms of similarity variables, this transforms to

$$\bar{R}(\eta) \to \bar{R}(\eta)\sqrt{1+\varepsilon\frac{2\cos(\theta)}{\bar{R}}e^{s/4}+\varepsilon^2\frac{1}{\bar{R}^2}e^{s/2}} \sim \bar{R}(\eta)+\varepsilon\cos(\theta)\,e^{s/4}+\mathcal{O}(\varepsilon^2) \tag{5.18}$$

The order ε contribution must satisfy the linearized similarity equation; we can identify the $m=1$ eigenmode (with $\theta_0=0$) as a constant,

$$\mathscr{L}^1(\bar{R}_i)\,1 = \tfrac{1}{4}(1)$$

producing the x-translational eigenfunction $\hat{R}^1_{i,\,X}(\eta)\equiv 1$ with eigenvalue $\lambda_X = 1/4$. A similar calculation produces the y-translation eigenfunction; the symmetry produces a change of variables given by replacing $\cos(\theta)$ with $\sin(\theta)$ in Eq. (5.18). Consequently, we identify the analogous $m=1$ eigenmode with $\theta_0=\pi/2$, given by $\hat{R}^1_{i,\,Y}(\eta)\equiv 1$ with eigenvalue $\lambda_Y = 1/4$.

There are also two eigenmodes associated with rotation, describing yawing and pitching of the axis. Because the rotational symmetries are invariant under the resealing, the associated eigenvalues are zero. The $x-z$ *rotation symmetry* is given by

$$x \to x\cos(\varepsilon)+z\sin(\varepsilon) \qquad z \to -x\sin(\varepsilon)+z\cos(\varepsilon) \tag{5.19}$$

transforming into the similarity variables and linearizing in ε yields

$$\bar{R}(\eta) \to \bar{R}(\eta)+\varepsilon(\eta-\bar{R}\bar{R}')\cos\theta+\mathcal{O}(\varepsilon^2) \tag{5.20}$$

The order ε contribution must satisfy the linearized similarity equation; we can identify the $m=1$ eigenmode (with $\theta_0=0$), producing the $x-z$ rotation eigenfunction $\hat{R}^1_{i,\,XZ}(\eta)\equiv\eta-\bar{R}\bar{R}'$ with eigenvalue $\lambda_{XZ}=0$. A similar calculation produces the $x-y$ rotation eigenfunction with $m=1$ and $\theta_0=\pi/2$, given by $\hat{R}^1_{i,\,Y}(\eta)\equiv\eta-\bar{R}\bar{R}'$ with eigenvalue $\lambda_Y = 1/4$.

Aside from these symmetry modes, any unstable angular eigenmodes would destabilize the similarity solutions found above. We are most interested in the full stability of the unique axisymmetricstable solution $\bar{R}_0(\eta)$. Our numerical computations show that all eigenvalues are real and negative aside from the anomalous eigenvalues associated with the symmetries (see Fig. 16). Thus, *the unique similarity solution stable to axisymmetric perturbations is also stable to nonaxisymmetric perturbations.*

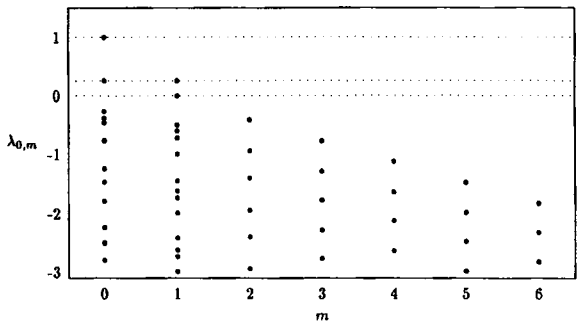

Fig. 16. Eigenvalues for non-axisymmetric eigenmodes with angular dependence $e^{im\theta}$ for the stable axisymmetric similarity solution $\bar{R}_0(\eta)$. The nonnegative eigenvalues are all associated with translation and rotation symmetries of the solution.

Our numerical investigation of the other similarity solutions $\bar{R}_i(\eta)$, $i = 1, 2, \ldots$ found no unstable modes for the non-axisymmetric ($m \geq 1$) perturbations. This suggests that simple axisymmetric evolution is the dominant behavior in cylindrical geometries.

6. DYNAMICS AFTER PINCHOFF

In the previous sections we considered the dynamics leading up to pinchoff. Exactly at pinchoff the local instantaneous structure of the solution is thought to be that of a double cone [WMVD98], $r_c(z) = c_0 |z - z_c|$ as $z \to z_c$. For times after pinchoff the solutions separates into two bodies. No proof is available to describe the continuation of the solution through this topological singularity, but it is possible to solve the surface diffusion problem in the new geometry for any finite time after pinchoff.

To describe the two pinched-off volumes it becomes more convenient to express the surfaces in the form $z = z(r, t)$. The equation of motion for the surfaces can then either be derived directly from (2.3) or from (3.4) using an inversion of variables to yield the equation

$$\frac{\partial z}{\partial t} = -\frac{1}{r}\frac{\partial}{\partial r}\left[\frac{r}{\sqrt{1+z_r^2}}\frac{\partial}{\partial r}\left(\frac{z_r}{r\sqrt{1+z_r^2}} + \frac{z_{rr}}{(1+z_r^2)^{3/2}}\right)\right] \tag{6.1}$$

As in the situation before pinchoff, we can obtain solution of (6.1) in terms of the similarity variables

$$z(r, t) = z_c + \tau^{1/4} Z(\rho, s) \qquad \rho = r\tau^{-1/4} \qquad \tau = t - t_c \qquad s = \ln(\tau) \tag{6.2}$$

satisfying the similarity partial differential equation,

$$Z_s - \frac{1}{4}(\rho Z_\rho - Z) = -\frac{1}{\rho}\left[\frac{\rho}{\sqrt{1+Z_\rho^2}}\left(\frac{1}{\rho}\left\{\frac{\rho Z_\rho}{\sqrt{1+Z_\rho^2}}\right\}_\rho\right)_\rho\right]_\rho \tag{6.3}$$

for $Z(\rho)$ defined on $0 \leqslant \rho < \infty$. For post-pinchoff behavior to be localized to the neighborhood of z_c, the similarity solution must take the form of a cone, $\bar{Z}(\rho) \sim b\rho$ in the far-field, with $b = 1/c$, and from (6.3) we obtain the expansion,

$$\bar{Z}(\rho) \sim b\rho\left(1 - \frac{1}{(1+b^2)\,\rho^4} + \frac{15(b^2+15)}{2(1+b^2)^3\,\rho^8} + \mathcal{O}(\rho^{-12})\right) \tag{6.4}$$

Using a WKB expansion as was done in Section 4, the linearized behavior of solutions in the far-field can be expressed as $\bar{Z}(\rho) \sim b\rho + w(\rho)$, where $w_0(\rho) \sim \rho$, or one of the three exponential modes,

$$w_m(\rho) \sim \rho^{-5/3} \exp(\tfrac{3}{4}\,\alpha_m[\tfrac{1}{4}(1+b^2)^2\,\rho^4]^{1/3}), \qquad m = 1, 2, 3 \tag{6.5}$$

and $\alpha_1 = 1$, $\alpha_{2,3} = (-1 \pm i\sqrt{3})/2$. The suppression of the exponentially growing mode $m = 1$ requires only two boundary conditions. Thus the solution is under-specified and we expect a continuum of solutions to exist. As per (6.4), numerical calculation of steady solutions of (6.3) yields a continuous family of solutions parametrized by the far-field slope b. Continuity of the far-field structure of the similarity solution with the slope $c_0 \approx 1.037$ of $\bar{R}_0(\eta)$ from before pinchoff suggests the solution with $b \approx 0.964$ [WMVD98]. Similarity solutions for different values of b are shown in Fig. 17, along with a schematic diagram of the geometry.

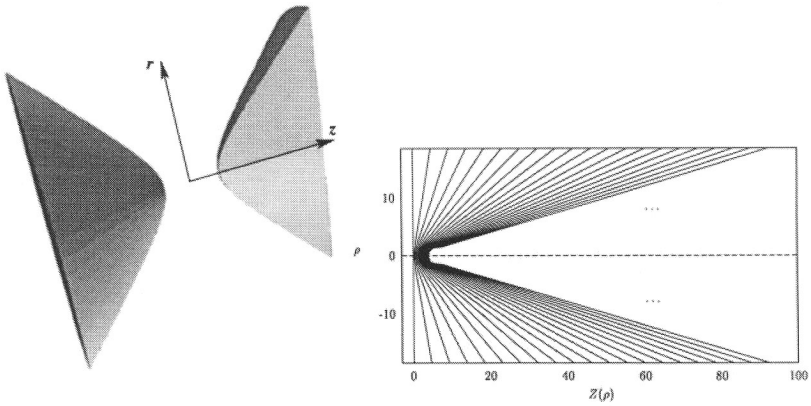

Fig. 17. The geometry after topological break-off and the continuous family of after-pinchoff similarity solutions.

We begin the analysis of the stability of these solutions over a range of possible values for b by considering the limit $b \to 0$. The limit $b \to 0$ is a flat surface, $z(r, t) = z_c$, about which we can linearize (6.1) $z(r, t) = z_c + \varepsilon f(r)\, e^{\sigma t}$ to obtain

$$\sigma f + \frac{1}{r}\frac{d}{dr}\left[r \frac{d}{dr}\left(\frac{1}{r}\frac{d}{dr}\left\{ r \frac{df}{dr} \right\}\right)\right] = 0 \tag{6.6}$$

This equation is an axisymmetric biharmonic equation, $\sigma f + \nabla^4 f = 0$, and can be solved in terms of Hankel transforms to yield

$$z(r, t) = z_c + \int_0^\infty \hat{f}_0(k)\, e^{-k^4(t-t_c)} J_0(kr)\, k\, dk \tag{6.7}$$

with the dispersion relation $\sigma = -k^4$. For analytic initial data that is exponentially localized to a neighborhood of the origin $r = 0$, the Hankel transform can be written as a Taylor series,

$$\hat{f}_0(k) = \sum_{n=0}^{\infty} a_n k^{2n} \tag{6.8}$$

By substituting (6.8) into (6.7), letting $\omega = k\tau^{1/4}$ and using (6.2), we obtain the solution in terms of similarity variables as

$$Z(\rho, s) = \sum_{n=0}^{\infty} a_n \hat{Z}_n(\rho)\, e^{\lambda_n s} \tag{6.9}$$

where

$$\hat{Z}_n(\rho) = \int_0^\infty \omega^{2n+1} e^{-\omega^4} J_0(\rho\omega)\, d\omega, \qquad \lambda_n = -\frac{2n+3}{4} \tag{6.10}$$

Equation (6.93) is an eigenfunction expansion with a countably infinite set of real, stable eigenmodes (6.10). Numerical calculation of the linear stability for similarity solutions at finite b shows that the spectrum remains discrete and stable but does not continue to be purely real, and hence we can conclude that the linear operator is not self-adjoint in general. As b increases, more and more pairs of real eigenvalues coalesce to form complex conjugate pairs (see Fig. 18).

In addition to the axisymmetric eigenmodes enumerated by (6.10) there are also two symmetry modes. Equation (6.1) is invariant under translations in space and time. Applying these invariant transformations to

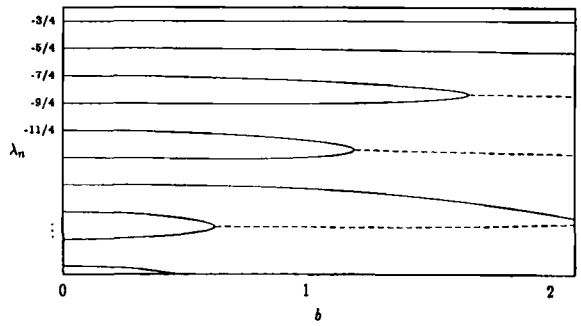

Fig. 18. Linear stability of the post-pinchoff similarity solutions: a plot of the eigenvalues as a function of the far-field slope b, dashed lines indicate the real parts of complex conjugate pairs.

the steady-profile similarity solutions $\bar{Z}(\rho)$ yields the linearized eigenmodes; for spatial translations $z \to z + \varepsilon$,

$$\hat{Z}_Z(\rho) = 1, \qquad \lambda_Z = -\tfrac{1}{4} \tag{6.11}$$

and for time-shifts, $t \to t + \varepsilon$,

$$\hat{Z}_T(\rho) = \tfrac{1}{4}(\rho \bar{Z}_\rho - \bar{Z}), \qquad \lambda_T = -1 \tag{6.12}$$

These eigenmodes have algebraic behavior in the far-field and will not occur in the expansion of strongly localized initial data. The stability of these symmetry modes, in contrast to the results in Section 5 before pinchoff, shows that the significance of errors in the assumed values for the critical position and time (z_c, t_c) decreases as time increases after pinchoff [WB98].

The uniqueness and stability of the after-pinchoff similarity solutions $\bar{Z}(\rho)$ for each cone-angle $\phi = \cot^{-1}(b)$ strongly suggests that there is a unique local continuation of the solution through the topology transition.

7. CONCLUSIONS

In this paper we examine the dynamics of solid filaments evolving via surface diffusion. We use a well-known model in which the normal velocity at the surface is proportional to the Laplacian of the mean-curvature [CT94]. This flow preserves the volume of the solid while minimizing surface area, corresponding to a minimization of surface energy. Cylindrical filaments are unstable to long-wave perturbations, analogous to the Rayleigh instability of fluid dynamics. This instability eventually lead to a conically self-similar pinchoff, leading to a loss of regularity and suggesting

a topological transition [CFM96, CFM95]. A plausible continuation after this pinchoff is that the cylinder is replaced by a chain of isolated spheres.

Section 2 related surface diffusion evolution to the problem of volume-constrained surface area minimization. We show that the linear stability of surface diffusion equilibria is equivalent to classifying the nature of the extrema for the capillary minimization problem. For axisymmetric equilibria, the only stable surfaces (where we restrict ourselves to single-valued non-zero radii) on a periodic interval are cylinders whose length is less than 2π times their radius; this is exactly the Rayleigh stability criterion as can be seen through the analogy with the capillary minimization problem. A family of unstable axisymmetric surfaces, Delaunay unduloids, exist which play a role in the dynamics. Through the analogy to capillary minimization, stability of equilibria can be determined by considering a second-order, self-adjoint operator as opposed to the fourth-order linearized surface diffusion operator. The connection to capillary minimization can be exploited for other geometries; for example, McCallum et al considered the stability of lines on an impermeable substrate [WMD97] and Wong et al consider the stability of substrates with catenoidal holes [WMD97]. This connection should also apply to the triply periodic family of gyroids, constant mean curvature surfaces recently constructed by Grosse-Brauckmann [GB97], an interesting point of study for surface diffusion in this geometry.

Section 3 discussed the nonlinear dynamics near axisymmetric equilibria. A combination of the stability results above, bifurcation theory and numerical simulation, gave a dynamical picture for the evolution of nearly cylindrical initial conditions on periodic intervals. For Rayleigh unstable intervals, perturbed cylinders decrease surface area until a pinchoff occurs [CFM96]. As the length of the interval decreases through the instability threshold, a branch of unstable Delaunay unduloids bifurcate from the cylinder. Bifurcation theory shows that locally this unstable solution and its stable manifold form the boundary between the basin of attraction of the stable cylinder and the basin of attraction of the topological pinchoff. Numerically we establish that this picture qualitatively remains the same for shorter intervals until the unduloid solution ceases to exist. Solutions evolve toward the cylinder (when it is a stable surface area minimizer) or towards pinchoff in an attempt to form a sphere, which is always a surface area minimizer. We showed that below the threshold for Rayleigh instability of the cylinder, there exists a regime where the cylinder is finite-amplitude unstable to perturbations that will lead to pinchoff. Above the critical wavelength for Rayleigh instability there may be additional dynamics that interact with the formation of singularities. It would be interesting to search for coarsen instabilities or competition between different global solutions leading to different critical times and positions for pinchoff.

Finite-time pinchoff singularities and changes in topology occur in many problems in continuum mechanics and differential geometry. Many studies of this phenomena in fluid problems were carried out recently at the University of Chicago, in particular the examination of thin films flows under the direction of Leo Kadanoff [CDG+93, DGKZ93, BBDK94]. These works stimulated new interest in formation of singularities through self-similar dynamics in higher order problems and generated valuable new analytical and numerical techniques for their study. Our work continues along this program. For the axisymmetric surface diffusion problem, we showed, in Section 4, that the similarity solution found by Wong *et al.* [WMVD98] is the first of a countably infinite set of symmetric similarity solutions. This kind of structure was recently observed by Brenner *et al.* [BLS96] for similarity solutions describing droplet pinchoff. Moreover, the first solution is the only one observed numerically. We found numerical agreement with the similarity solution over many decades of data, in the spirit of [BB95, Ber96, BBDK94, Ber95]. Some interesting theoretical questions arise from this study. Can one prove that the set of similarity solutions constructed numerically here are the only similarity solutions with this scaling? Also, to date, no one has proved rigorously that finite-time pinchoff occurs in this problem.

In Section 5, we developed a stability theory for self-similar solutions. The linear stability of the similarity solutions can be related to an eigenvalue problem in the similarity variables. The temporal and spatial translation symmetries of the problem give rise to anomalous positive eigenvalues in the spectrum; when the symmetries are properly accounted for, we find that the first similarity solution is the only stable solution and that the nth solution has $2(n-1)$ unstable directions. This result accounts for only the first solution being observed. We verify the stability theory by investigating the evolution of an unstable similarity solution numerically. In addition, we compute the stability of the solution to non-axisymmetric perturbations; once the additional translation and rotation symmetries are accounted for, we conclude that the first solution is also the only solution stable to non-axisymmetric perturbations. We believe the stability theory developed here provides a template for examining linear stability in the setting of self-similarity and determining selection when multiple similarity solutions exist.

In Section 6, we consider the existence and stability of solutions after pinchoff. We find a continuous family of stable similarity solutions parametrized by the far-field cone angle. These results suggest that the continuation after pinchoff is unique.

While the surgery technique used by Coleman, Falk, and Moakher [CFM95] allows them to transition through pinchoff, it does not address

the issue of uniqueness of continuation. Eggers' [Egg98] study of the coalescence of spheres uses a similar ad hoc regularization and symmetry to continue the evolution past subsequent coalescences of the interfaces. The continuation of the surface through topological transition has been widely studied for the related problem of motion by mean curvature. Evans and Spruck [ES91] and Chen, Giga and Goto [CGG91] showed that mean curvature motion has a unique continuous *viscosity* solution. Instead of considering the motion of a single surface, they embed the initial condition as a level-set of a function in space. They then introduce a viscous diffusion term, and show the evolution of the level-set equation is unique and smooth in the limit of vanishing viscosity. Altschuler, Angenent and Giga [AAG95] and Soner and Souganidis [SS93] both studied the regularity of bounded axisymmetric surfaces shrinking via mean-curvature flow. They showed (with some technical restrictions) that the unique viscous solution is smooth except at a finite number of critical times at which pinchoff occurs, and that the pinchoff occurs in the manner described by Huisken [Hui90], in which a rescaled solution approaches a cylinder.

Because motion via surface diffusion is fourth-order in space, the tools used for the second-order parabolic system arising from mean-curvature motion are generally insufficient (see the discussion in [CT94]). One possible method of defining a unique continuation is again to equate the motion of the surface with the level-set of a function defined throughout space. Cahn, Elliot, and Novick–Cohen [CENC96] presented a Cahn–Hilliard model with a degenerate mobility that formally yields motion by the Laplacian of mean-curvature for its zero level set in a diffusive boundary layer limit. Elliot and Garcke [EG96] proved the existence of weak solutions for this class of Cahn–Hilliard equations. A challenging problem for further study would be to use this formulation to analyze pinchoff, intersection of interfaces, or any other loss of regularity issues that arise in motion via surface diffusion. Clearly surface diffusion is a problem with a rich and complex set of dynamics that we have only just begun to understand.

APPENDIX. NUMERICAL METHOD FOR SIMULATIONS OF PINCHOFF

Here we describe the numerical method used to perform self-similar adaptive mesh refinement calculations of the initial pinchoff singularity. Previous numerical work on this problem includes that of [LC89, BT94, CFM96, CFM95].

We used a finite difference spatial discretization of Eq. (3.4) in which the computational domain is divided into intervals with endpoints marked

by the nodes $z_1 < z_2 < \cdots < z_k$. The function $r(z, t)$ is approximated by its computed value r_i^j at the node z_i at time t_j. The mean curvature $\mathscr{H}$ of the interface is approximated at each node z_i by the finite difference approximation

$$\mathscr{H}_i = -\frac{1}{r_i \delta_i \tilde{r}_i \Delta z_{i+1/2}} \left(\frac{\tilde{r}_i}{\sqrt{1+\delta r_i^2}} - \frac{\tilde{r}_{i-1}}{\sqrt{1+\delta r_{i-1}^2}} \right) \tag{A.1}$$

where

$$\Delta z_i = z_{i+1} - z_i \qquad \Delta z_{i+1/2} = \frac{1}{2}(z_{i+1} - z_{i-1})$$

$$\Delta r_i = r_{i+1} - r_i \qquad \delta r_i = \frac{\Delta r_i}{\Delta z_i}$$

$$\tilde{r}_i = \frac{1}{2}(r_i + r_{i+1}) \qquad \delta \tilde{r}_i = \frac{1}{2}(\delta r_i + \delta r_{i+1})$$

Expression (A.1) is a finite difference discretization of the exact differential for the mean curvature (3.6)

$$\mathscr{H} = -\frac{1}{r r_z} \left(\frac{r}{\sqrt{1+r_z^2}} \right)_z$$

This approximation works very well across changes in grid size except near points where r_z gets small. There, round-off error introduces some instabilities into the code. This problem is easily resolved by replacing (A.1) by an asymptotic approximation (with r_z as the small parameter) for numerical values of r_z below a threshold.

The PDE is then solved implicitly on each time-step using a backward Euler method:

$$\frac{(r_i^{j+1})^2 - (r_i^j)^2}{2\,\Delta t_j} + \frac{f(r_{i+1}^{j+1}, r_i^{j+1}, \Delta z_i)\, v_i^{j+1} - f(r_i^{j+1}, r_{i-1}^{j+1}, \Delta z_{i-1})\, v_{i-1}^{j+1}}{\Delta z_{i+1/2}} = 0 \tag{A.2}$$

where the flux terms f and v are defined by

$$f(s, y, dz) = \frac{x+y}{2\sqrt{1+((x-y)/dz)^2}} \qquad v_i^{j+1} = \frac{3(\mathscr{H}_{i+1}^{j+1} - \mathscr{H}_i^{j+1})}{\Delta z_{i-1} + \Delta z_i + \Delta z_{i+1}} \tag{A.3}$$

and $\Delta t_j \equiv t_{j+1} - t_j$ denotes the new time-step. Note that when the implicit Eq. (A.2) is solved exactly and a fixed grid is used, the scheme conserves the discrete approximation of the volume

$$\sum_i \tfrac{1}{2}(r_i^j)^2 \, \Delta z_{i+1/2}$$

The time-step is chosen adaptively, based on a need to satisfy an error tolerance and a maximum relative decrease in the minimum of the solution. The coupled Eqs. (A.2)–(A.3) are solved using a Newton iteration. The actual code is adapted from ones used to compute lubrication type equations and MKS equations in [Ber96, BBDK94, BB95, BP98].

The initial grid is uniform in space. The grid is adaptively refined in a self-similar fashion using the technique outlined in [Ber96] for lubrication-type equations. The main idea is that when $r_{\min} = \min_i(r_i)$ goes below some threshold local grid refinement is performed by subdividing a fixed number of cells near the node z_i corresponding to $r_{\min}$. The mesh is then repeatedly refined in this fashion whenever the minimum goes below the next threshold. Some advanced knowledge of the relationship between the characteristic length-scale of the self-similarity and $r_{\min}$ is needed in order to effectively resolve the structure. In this case, we know $r_{\min} \sim l$ where l is the characteristic lengthscale of the pinch region. So, if we subdivide by a factor of two each time, then the regridding must be repeated whenever $r_{\min}$ decreases by a factor of two. When the mesh is subdivided new values of r and v are computed via linear interpolation for v and linear interpolation of second differences for r. Immediately after remeshing, the adaptive time-step is cut by a factor of 20 in order to smooth high frequency noise induced by the regridding. For more details about the adaptive mesh refinement, the reader is referred to [Ber96].

ACKNOWLEDGMENTS

During the past decade, Leo Kadanoff has spearheaded a large research effort, at the University of Chicago, directed at understanding the structure of finite-time singularities in nonlinear systems. It is a pleasure to write this paper for a special issue in honor of his 60th birthday.

A.L.B. thanks R. Falk and M. Moakher for first introducing her to the problem and for useful conversations. A.J.B. thanks Harris Wong, Mike Miksis, Matt McCallum, and Steve Davis for numerous discussions on their work on evolution via surface diffusion. We are particularly grateful to them for providing us with several preprints before their publication. A.J.B. also thanks John McCuan for discussions about the capillary minimization problem and Ted Shifrin for improving his geometrical insight

(and his appetite). An early version of the Newton–Raphson code used to solve the similarity ODE was developed by A.J.B. and W. Douglas Wilson on a related problem; although this work was never published the experienced gained was invaluable for understanding the stability of self-similar solutions. A.J.B. and A.L.B. acknowledge discussions with Robert Bryant whose encyclopedic knowledge helped us navigate the differential geometry.

This work is supported by the Office of Naval Research via a PECASE/YIP award. TPW is supported by an NSF postdoctoral fellowship. ALB is also partially supported by a Sloan Research Fellowship.

REFERENCES

[AAG95] Steven Altschuler, Sigurd B. Angenent, and Yoshikazu Giga, Mean curvature flow through singularities for surfaces of rotation, *J. Geom. Anal.* **5**(3):293–358 (1995).

[ABB96] Robert Almgren, Andrea L. Bertozzi, and Michael P. Brenner, Stable and unstable singularities in the unforced Hele-Shaw cell, *Phys. Fl.* **8**(6):1356–1370 (1996).

[AL98] Sergio A. Alvarez and Chun Liu, Motion of a closed curve by minus the surface Laplacian of curvature (1998).

[Ari62] R. Aris, *Vectors, Tensors, and the Basic Equations of Fluid Mechanics* (Dover Publications, Inc., 1962).

[Bar96] G. I. Barenblatt, *Scaling, Self-similarity, and Intermediate Asymptotics* (Cambridge University Press, New York, 1996).

[BB95] A. J. Bernoff and A. L. Bertozzi, Singularities in a modified Kuramoto–Sivashinsky equation describing interface motion for phase transition, *Physica D* **85**(3):375–404 (1995).

[BBDK94] Andrea L. Bertozzi, Michael P. Brenner, Todd F. Dupont, and Leo P. Kadanoff, Singularities and similarities in interface flow, in *Trends and Perspectives in Applied Mathematics*, Vol. 100, Applied Mathematical Sciences, L. Sirovich, ed. (Springer-Verlag, New York, 1994), pp. 155–208.

[BDR84] Pierre Baras, Jean Duchon, and Raoul Robert, Evolution d'une interface par diffusion de surface, *Comm. Partial Differential Equations* **9**(4):313–335 (1984).

[Ber95] A. L. Bertozzi, Loss and gain of regularity in a lubrication equation for thin viscous films, in *Free Boundary Problems. Theory and Applications*, Vol. 323, Pitman Research Notes in Mathematics Series, J. I. Diaz, M. A. Herrero, A. Linan, and J. L. Vazquez, eds. (Longman House, 1995), pp. 72–85. Proceedings of the International Colloquium on Free Boundary Problems, Toledo, Spain, June 1993.

[Ber96] Andrea L. Bertozzi, Symmetric singularity formation in lubrication-type equations for interface motion, *SIAM J. Applied Math.* **56**(3):681–714 (1996).

[BLS96] M. P. Brenner, J. R. Lister, and H. A. Stone, Breaking threads, similarity solutions and the number 0.0304, *Phys. Fluids* **8**:2827–2836 (1996).

[BO78] Carl M. Bender and Steven A. Orszag, *Advanced Mathematical Methods for Scientists and Engineers* (McGraw-Hill, Inc., New York, 1978).

[BP98] A. L. Bertozzi and M. C. Pugh, Long-wave instabilities and saturation in thin film equations, *Comm. Pure Appl. Math.* **LI**:625–661 (1998).

[BSS94] P. Basa, J. C. Schon, and P. Salamon, The use of Delaunay curves for the wetting of axisymmetric bodies, *Quarterly Appl. Math.* **52**(1):1–22 (1994).

[BT94] P. Broadbridge and P. Tritscher, An integrable fourth-order nonlinear evolution equation applied to thermal grooving of metal surfaces, *IMA J. Appl. Math.* **53**(3):249–265 (1994).

[But68] Eugene Butkov, *Mathematical Physics* (Addison-Wesley Pub. Co., Reading, MA, 1968).

[CDG+93] Peter Constantin, Todd F. Dupont, Raymond E. Goldstein, Leo P. Kadanoff, Michael J. Shelley, and Su-Min Zhou, Droplet breakup in a model of the Hele–Shaw cell, *Phys. Rev. E* **47**(6):4169–4181 (1993).

[CENC96] J. W. Cahn, C. M. Elliott, and A. Novick-Cohen, The Cahn–Hilliard equation with a concentration dependent mobility: Motion by minus the Laplacian of the mean curvature, *European J. Appl. Math.* **7**(3):287–301 (1996).

[CFM95] B. D. Coleman, R. S. Falk, and M. Moakher, Stability of cylindrical bodies in the theory of surface diffusion, *Physica D* **89**(1–2):123–135 (1995).

[CFM96] B. D. Coleman, R. S. Falk, and M. Moakher, Space-time finite element methods for surface diffusion with applicatlon to the theory of the stability of cylinders, *SIAM J. Sci. Comput.* **17**(6):1434–1448 (1996).

[CGG91] Yun Gang Chen, Yoshikazu Giga, and Shun'ichi Goto, Uniqueness and existence of viscosity solutions of generalized mean curvature flow equations, *J. Differential Geom.* **33**(3):749–786 (1991).

[CH93] M. C. Cross and P. C. Hohenberg, Pattern formation outside of equilibrium, *Rev. Mod. Phys.* **65**(3):854–1112 (1993).

[CS97] Y.-J. Chen and P. H. Steen, Dynamics of inviscid capillary breakup: Collapse and pinchoff of a film bridge, *J. Fluid Mechanics* **341**:245–267 (1997).

[CT94] J. W. Cahn and J. E. Taylor, Surface motion by surface diffusion, *Acta Metall. Mater.* **42**(4):1045–1063 (1994).

[Del41] C. E. Delaunay, Sur la surface de revolution dont la courbure moyenne est constante, *J. Math. Pures Appl.* **6**:309–320 (1841).

[DGKZ93] Todd F. Dupont, Raymond E. Goldstein, Leo P. Kadanoff, and Su-Min Zhou, Finitetime singularity formation in Hele–Shaw systems, *Phys. Rev. E* **47**(6): 4182–4196 (1993).

[Dre90] Donald A. Drew. Evolution of geometric statistics, *SIAM J. Appl. Math.* **50**(3):649–666 (1990).

[EG96] Charles M. Elliott and Harald Garcke, On the Cahn–Hilliard equation with degenerate mobility, *SIAM J. Math. Anal.* **27**(2):404–423 (1996).

[EG97] Charles M. Elliott and Harald Gareke, Existence results for diffusive surface motion laws, *Adv. Math. Sci. Appl.* **7**(1):467–490 (1997).

[Egg93] Jens Eggers, Universal pinching of 3D axisymmetric free surface flow, *Phys. Rev. Lett.* **71**:3458 (1993).

[Egg98] Jens Eggers, Coalescence of spheres by surface diffusion, *Phys. Rev. Lett.* **80**(12):2634–2637 (1998).

[EMS97] Joachim Escher, Uwe F. Mayer, and Gieri Simonett, On the surface diffusion flow. In *Proceedings of 6th International Conference on Navier–Stokes Equation and Related Nonlinear Problems, Palanga, Lithuania* (1997).

[EMS98] Joachim Escher, Uwe F. Mayer, and Gieri Simonett, The surface diffusion flow for immersed hypersurfaces (1998). To appear in *SIAM J Math. Anal.*

[ES91] L. C. Evans and J. Spruck, Motion of level sets by mean curvature. I, *J. Differential Geom.* **33**(3):635–681 (1991).

[Fin86] R. Finn, *Equilibrium Capillary Surfaces* (Springer-Verlag, New York, 1986).

[FK92] Stathis Filippas and Robert V. Kohn, Refined asymptotics for the blowup of $u_t - \delta u = u^p$, *Comm. Pure Appl. Math.* **45**(7):821–869 (1992).

[FV92] R. Finn and T. I. Vogel, On the volume infimum for liquid bridges, *Z. Anal. Anwendungen* **11**(1):3–23 (1992).

[GB97] Karsten Grosse-Brauckmann, Gyroids of constant mean curvature, *Experimental Mathematics* **6**(1):33–50 (1997).

[GK87] Yoshikazu Giga and Robert V. Kohn, Characterizing blowup using similarity variables, *Indiana Univ. Math. J.* **36**(1):1–40 (1987).

[GPS93] Raymond E. Goldstein, Adriana I. Pesci, and Michael J. Shelley, Topology transitions and singularities in viscous flows, *Phys. Rev. Lett.* **70**(20):3043–3046 (1993).

[GvL89] G. H. Golub and C. F. van Loan, *Matrix Computations* (Johns Hopkins, Baltimore, 1989).

[Her51] C. Herring, Surface diffusion as a motivation for sintering, in *The Physics of Powder Metallurgy*, Chapter 8, W. E. Kingston, ed. (McGraw-Hill, 1951), pp. 143–179.

[Hil76] F. B. Hildebrand, *Advanced Calculus for Applications*, 2nd ed. (Prentice-Hall, New Jersey, 1976).

[Hui90] Gerhard Huisken, Asymptotic behavior for singularities of the mean curvature flow, *J. Differential Geom.* **31**(1):285–299 (1990).

[Kad97] Leo P. Kadanoff, Singularities and blowups, *Physics Today*, p. 11, September 1997.

[LC89] J. K. Lee and T. H. Courtney, Two-dimensional finite difference analysis of shape instabilities in plates, *Metall. Trans. A* **20**:1385–1394 (1989).

[Man90] Paul Manneville, *Dissipative Structures and Weak Turbulence* (Academic Press, Inc., San Diego, CA, 1990).

[MS79] T. F. Marinas and R. F. Sekerka, A model for capillary induced instabilities in directionally solidified eutectic alloys, in *Conference on In Situ Composites-III*, J. L. Walter *et al.*, ed. (Ginn Custom Publishing, Lexington, MA, 1979), pp. 86–96.

[Mul57] W. W. Mullins, Theory of thermal grooving, *J. Appl. Phys.* **28**(3):333–339 (1957).

[Mul59] W. Mullins, Flattening of a nearly plane solid surface due to capillarity, *J. Appl. Phys.* **30**(1):77–83 (1959).

[Mul95] W. W. Mullins, Mass transport at interfaces in single component systems, *Metall. Trans. A* **26**:1917–1929 (1995).

[MVM+96] M. S. McCallum, P. W. Voorhees, M. J. Miksis, S. H. Davis, and H. Wong. Capillary instabilities in solid thin-films—lines, *J. Appl. Phys.* **79**(10):7604–7611 (1996).

[NM65a] F. A. Nichols and W. W. Mullins, Morphological changes of a surface of revolution due to capillarity-induced surface diffusion, *J. Appl. Phys.* **36**(6): 1826–1835 (1965).

[NM65b] F. A. Nichols and W. W. Mullins, Surface- (interface-) and volume-diffusion contributions to morphological changes driven by capillarity, *Trans. Metall. Soc. AIME* **233**:1840–1847 (1965).

[PTVF92] W. H. Press, S. A. Teukolsky, W. T. Vetterling, and B. P. Flannery, *Numerical Recipes in C*, 2nd ed. (Cambridge University Press, Cambridge, 1992).

[SB95] David C. Sarocka and Andrew J. Bernoff, An intrinsic equation of interfacial motion for the solidification of a pure hypercooled melt, *Physica D* **85**(3): 348–374 (1995).

[SM82] R. F. Sekerka and T. F. Marinas, Dynamics of morphological change during solid-solid transformations, in *Solid-solid Phase Transformations*, H. I. Aaronson *et al.*, ed. (The Metallurgical Society of AIME, New York, 1982), pp. 67–86.

[SS93] H. M. Soner and P. E. Souganidis, Singularities and uniqueness of cylindrically symmetric surfaces moving by mean curvature, *Comm. Partial Differential Equations* **18**(5–6):859–894 (1993).

[TC94] J. E. Taylor and J. W. Cahn, Linking anisotropic sharp and diffuse surface motion laws via gradient flows, *J. Stat. Phys.* **77**(1–2):183–197 (1994).

[Vog87] Thomas I. Vogel, Stability of a liquid drop trapped between two parallel planes, *SIAM J. Appl. Math.* **47**(3):516–525 (1987).

[Vog89] Thomas I. Vogel, Stability of a liquid drop trapped between two parallel planes, II. General contact angles, *SIAM J. Appl. Math.* **49**(4):1009–1028 (1989).

[War83] Frank W. Warner, *Foundations of Differentiable Manifolds and Lie Groups*, Vol. 94, Graduate Tezts in Mathematics (Springer-Verlag, New York/Berlin, 1983). Corrected reprint of the 1971 edition.

[Way97] C. Eugene Wayne, Invariant manifolds for parabolic partial differential equations on unbounded domains, *Arch. Rational Mech. Anal.* **138**(3):279–306 (1997).

[WB98] T. P. Witelski and A. J. Bernoff, Self-similar asymptotics for linear and nonlinear diffusion equations, *Studies in Applied Mathematics* **100**(2):153–193 (1998).

[WMD97] H. Wong, M. J. Miksis, and S. H. Davis, Capillarity driven motion of solid film wedges, *Acta Mater.* **45**(6):2477–2484 (1997).

[WMVD98] H. Wong, M. J. Miksis, P. W. Voorhees, and S. H. Davis, Universal pinch off of rods by capillarity-driven surface diffusion (1998). *Scripta Mater.* **39**(1):55–60 (1998).

[WVMD97] H. Wong, P. W. Voorhees, M. J. Miksis, and S. H. Davis, Capillary instabilities of a catenoidal hole in a soild film, *J. Appl. Phys.* **81**(9):6091–6099 (1997).

[Zho93] L. Zhou, On the volume infimum for liquid bridges, *Z. Anal. Anwendungen* **12**(4):629642 (1993).